BRAIN CONNECTIVITY
Volume 1, Number 6, 2011
© Mary Ann Liebert, Inc.
DOI: 10.1089/brain.2011.0071

REVIEW ARTICLE

Characterization of Cerebral White Matter Properties Using Quantitative Magnetic Resonance Imaging Stains

Andrew L. Alexander,[1–3] Samuel A. Hurley,[1] Alexey A. Samsonov,[4]
Nagesh Adluru,[3] Ameer Pasha Hosseinbor,[1,3] Pouria Mossahebi,[5] Do P.M. Tromp,[3]
Elizabeth Zakszewski,[1,3] and Aaron S. Field[4,5]

Abstract

The image contrast in magnetic resonance imaging (MRI) is highly sensitive to several mechanisms that are modulated by the properties of the tissue environment. The degree and type of contrast weighting may be viewed as image filters that accentuate specific tissue properties. Maps of quantitative measures of these mechanisms, akin to microstructural/environmental-specific tissue stains, may be generated to characterize the MRI and physiological properties of biological tissues. In this article, three quantitative MRI (qMRI) methods for characterizing white matter (WM) microstructural properties are reviewed. All of these measures measure complementary aspects of how water interacts with the tissue environment. Diffusion MRI, including diffusion tensor imaging, characterizes the diffusion of water in the tissues and is sensitive to the microstructural density, spacing, and orientational organization of tissue membranes, including myelin. Magnetization transfer imaging characterizes the amount and degree of magnetization exchange between free water and macromolecules like proteins found in the myelin bilayers. Relaxometry measures the MRI relaxation constants T1 and T2, which in WM have a component associated with the water trapped in the myelin bilayers. The conduction of signals between distant brain regions occurs primarily through myelinated WM tracts; thus, these methods are potential indicators of pathology and structural connectivity in the brain. This article provides an overview of the qMRI stain mechanisms, acquisition and analysis strategies, and applications for these qMRI stains.

Key words: diffusion; magnetic resonance imaging; magnetization transfer; myelin; relaxometry; white matter

Introduction

Brain function requires efficient and effective communications between different brain regions and between the brain and body. Recent developments in magnetic resonance imaging (MRI), electro-encephalography (EEG), and magneto-encephalography (MEG) methods have enabled researchers to study the brain as a collection of networks rather than isolated regions. The applications of functional connectivity mapping using resting blood-oxygen-level-dependent (BOLD) functional MRI (fMRI) for mapping functional brain networks are the most rapidly growing neuroimaging methods. These functional networks may be modulated by the white matter (WM) substrates that conduct the electrical signal between different regions of the central nervous system (CNS). In this article we will review several methods that are being used to characterize WM properties.

WM primarily consists of densely bundled nerve fibers, each comprising an axon extending from the neuronal cell body with a long, narrow, cylindrical geometry and surrounded by a myelin sheath. The main role of axons is to conduct electrical signals from the cell body to other neurons. This signal conduction is enhanced by the myelin sheath, which consists of concentric layers of lipids and proteins that insulate the axon while also providing mechanical and biochemical support. The axon at its distal end interfaces with other cells (primarily other neurons) and transmits signals by way of chemical neurotransmitters across synaptic junctions. Other cell types in the WM include the oligodendrocytes that synthesize and maintain myelin as well as astrocytes (biochemical

Departments of [1]Medical Physics and [2]Psychiatry, University of Wisconsin, Madison, Wisconsin.
[3]Waisman Laboratory for Brain Imaging and Behavior, University of Wisconsin, Madison, Wisconsin.
Departments of [4]Radiology and [5]Biomedical Engineering, University of Wisconsin, Madison, Wisconsin.

support) and other support glia. Injured or inflamed CNS WM may also contain microglia and macrophages.

Noninvasive imaging techniques that can characterize WM tissue properties and reveal changes induced by healthy development and aging, genetics, disease, and injury are potentially valuable. Ideally, quantitative imaging measures that are indicators of specific changes—for example, myelination, axonal changes, gliosis, inflammation—would be useful for a broad range of clinical and research applications and would improve our understanding of how WM properties influence the function of brain networks. A major challenge is that the spatial resolution of quantitative MRI (qMRI) is currently on the order of millimeters, whereas axonal diameters range from 1 to 20 μm and the thickness of the healthy myelin sheath is on the order of 1 μm. Consequently, MRI can provide only a macroscopic picture of contrast weighting mechanisms that are sensitive and ideally specific to the WM microstructural properties of interest.

In this article, we will review three qMRI techniques—diffusion MRI (including diffusion tensor imaging [DTI]), magnetization transfer (MT), and multicomponent relaxometry—for characterizing WM properties with an emphasis on myelin. These qMRI methods generate image maps with individual signal contrast or stains, which are potential biomarkers of myelin- and axon-related changes in WM. Each of these stains relies on unique mechanisms influenced by how water in tissue interacts with its environment at the molecular, cellular, and/or tissue microstructural level. For each stain, we will review the underlying mechanisms, methods for measurement, relative merits, and key drawbacks. We will also briefly discuss other potential MRI methods for characterizing WM. Finally, we will attempt to summarize the current state of the field and make some recommendations regarding potential directions of research and development in this area.

Diffusion MRI

Mechanisms and measurement methods

Currently, the most widely used imaging method to study and characterize WM in a broad range of diseases and disorders is DTI, which is highly sensitive to variations in the tissue microstructure. Diffusion MRI is sensitive to the random motion of water molecules in a medium (Le Bihan et al., 1991a). The image signal in a diffusion-weighted imaging (DWI) study is modulated by the presence, orientation, and density of membranes and other barriers in the tissue (Fig. 1). As the density of the barriers increases or the spacing between barriers decreases, the water diffusion will be more hindered (Beaulieu and Allen, 1994; Norris et al., 1994). Diffusion measurements that are modulated by the barriers in tissue are often referred to as apparent diffusion coefficients. In fibrous tissues like WM and skeletal muscle, the density of the barriers is much higher in the direction perpendicular to the fibers; thus, the apparent diffusivity is much higher in the direction parallel to the fiber bundles than in the perpendicular orientation (Chenevert et al., 1990; Moseley et al., 1991). Diffusion MRI appears to be highly sensitive to the effects of tissue cellularity, cellular swelling, axonal injury and loss, myelination, edema, necrosis, and inflammation [see Alexander et al. (2007) for review]. DWI and DTI pulse sequences and simple analysis tools are now available on all modern clinical scanner platforms.

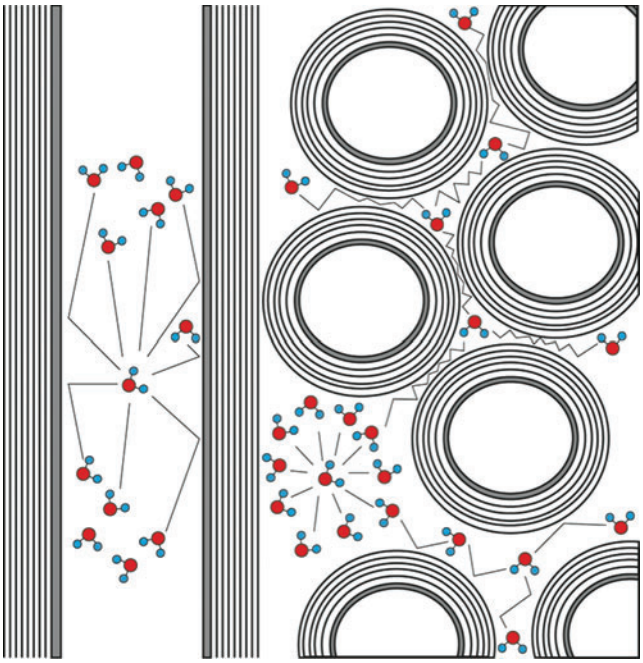

FIG. 1. Schematic illustration of water diffusion interacting with myelinated axons. The apparent diffusion is greatest in the direction parallel to the axons (left side). The diffusion distances and corresponding apparent diffusion coefficient are reduced for more densely packed axons (right side).

The basis for nearly all DWI and DTI clinical and research studies is a pulsed-gradient, spin-echo, echo-planar imaging (EPI) sequence (Le Bihan et al., 1991b), where the diffusion-encoding gradients bracket the refocusing (RF) pulse(s). The basic signal model for DWI is

$$S = S_o\, e^{-bD} \quad (1),$$

with diffusion weighting (Le Bihan et al., 1991b; Stejskal and Tanner, 1965)

$$b = (\gamma G \delta)^2 (\Delta - \delta/3) \quad (2),$$

where S_o is the signal without diffusion-weighting gradients ($b = 0$), D is the apparent diffusion coefficient, γ is the gyromagnetic ratio, G is the diffusion gradient amplitude, δ is the width of the diffusion gradient pulses, and Δ is the time between diffusion gradients. Since the maximum diffusion gradient on clinical MRI scanners is limited (currently 4–8 G/cm), the width of the gradients has to be long to achieve high diffusion-weighting.

An elegant MRI method for characterizing the anisotropic diffusion of water in biological tissues is DTI, which was originally described by Peter Basser and colleagues at NIH in 1994 (Basser et al., 1994). The primary assumption of DTI is that the probability density of displacements from diffusion is a three-dimensional (3D) multivariate Gaussian distribution, where the diffusion tensor is the covariance matrix of diffusion displacements

$$\mathbf{D} = \begin{pmatrix} D_{XX} & D_{XY} & D_{XZ} \\ D_{YX} & D_{YY} & D_{YZ} \\ D_{ZX} & D_{ZY} & D_{ZZ} \end{pmatrix} \quad (3)$$

The Gaussian diffusion distribution described by the diffusion tensor may be represented by a 3D ellipsoid with the

lengths and orientations of the major, medium, and minor axes corresponding to the eigenvalues and eigenvectors of the diffusion tensor.

There are many factors associated with the image acquisition of DTI data that will influence the measurements, including the pulse sequence design and parameters (Le Bihan et al., 1991b) (i.e., single vs. dual echo, parallel imaging, repetition time [TR], and echo time [TE]), DTI encoding parameters (diffusion-weighting and encoding directions), factors that influence the signal-to-noise ratio (SNR) such as the B0 magnetic field strength, gradient performance and coil sensitivity, and artifacts including pulsatile (e.g., cardiac) signal fluctuations, ghosting, and distortions from B0 field inhomogeneities and eddy currents; see Alexander et al. (2007) and Tournier et al. (2011) for reviews. For most research applications in the human brain, it is desirable to obtain isotropic spatial resolution. At 1.5T and 3.0T, target resolutions of 2.5 mm and 2.0 mm, respectively, are commonly used and achievable. A DTI protocol with 30–40 encoding directions at $b = 1000\,\mathrm{sec/mm^2}$ and 4–6 averages of $b = 0$ at a resolution of 2 mm at 3.0T will achieve good quality DTI maps in many cases though more averaging will improve the measurement accuracy and variance.

The processing of DWI data requires careful inspection of the DW images, correction of artifacts, and tools for obtaining regionally specific measures. If rotation or shear is detected in a DW image volume, ideally the gradient direction should also be adjusted to account for differences in the encoding frame. It has been reported that corrections to the encoding directions after motion and eddy current distortion correction can lead to significant changes in the estimated diffusion tensor measures (Leemans and Jones, 2009). For DTI studies, the diffusion tensor is often estimated using a linear least squares or weighted least squares approach, though a nonlinear least squares approach has been shown to yield the most robust fit in noisy data (Jones and Basser, 2004; Koay et al., 2006). In the case where artifactual noise may be present, robust estimators may be used to identify and either remove or minimize the impact of outlier measurements (RESTORE) (Chang et al., 2005).

One of the greatest confounds in DWI is partial volume averaging between tissue components. The relatively large voxel sizes used in most DWI studies can lead to multiple tissue types (e.g., cerebral spinal fluid [CSF], WM, and gray matter [GM]) within a voxel (Alexander et al., 2001). Further, disease processes like edema and infiltrating tumor can make it difficult to accurately characterize the underlying WM fiber properties. Also, regions of crossing or highly divergent WM fibers will affect the diffusion tensor eigenvalues and diffusion anisotropy measures. In fact in regions of crossing WM tracts, the simple diffusion tensor model is not adequate for characterizing the tissue microstructure (Alexander et al., 2001).

DTI measures

Diagnonalization of the tensor gives us the eigenvalues (λ_1, λ_2, and λ_3 in decreasing order of magnitude) and the corresponding eigenvectors ($\boldsymbol{e_1}$, $\boldsymbol{e_2}$, and $\boldsymbol{e_3}$). Many different stains may be derived from the eigenvalues, which are invariant to the tensor orientation [e.g., Alexander et al. (2000); Basser (1997); Ennis and Kindlmann (2006); Westin et al. (2002)]. How the eigenvalues are combined and weighted can be viewed as different filters for accentuating specific features of the water diffusion. Commonly used DTI measures include the mean diffusivity (*MD*) and the fractional anisotropy (*FA*) (Basser and Pierpaoli, 1996; Pierpaoli and Basser, 1996) (also see Fig. 2):

$$MD = (\lambda_1 + \lambda_2 + \lambda_3)/3 \tag{4}$$

$$FA = \sqrt{\frac{3}{2}\frac{(\lambda_1 - MD)^2 + (\lambda_2 - MD)^2 + (\lambda_3 - MD)^2}{\lambda_1^2 + \lambda_2^2 + \lambda_3^2}} \tag{5}$$

MD and *FA* describe complementary information about the diffusion of water. The specific interpretation of all diffusion measures needs to be kept within the context of the diffusion mechanism, which is the modulation of the diffusion coefficient of free water by tissue membranes. *FA* is a normalized standard deviation of the eigenvalues and is commonly referred to as a summary measure of microstructural integrity. While *FA* is highly sensitive to microstructural changes, it is not very specific to the type of change and it is highly advisable to also include other DTI measures in any analysis. At a minimum, studies should include the *MD*, which is the directionally averaged, inverse measure of the membrane density and fluid viscosity and is very similar for both GM and WM, particularly at $b \sim 1000\,\mathrm{sec/mm^2}$. *MD* is sensitive to cellularity, edema, and necrosis. It is important to understand that noise in the measured signals can lead to overestimates of the diffusion anisotropy, particularly in more isotropic regions (Pierpaoli and Basser, 1996). Thus, SNR is an important factor to consider in the interpretation of noisy DTI data.

The apparent diffusivities in the directions parallel and perpendicular to the WM tracts are the axial and radial diffusivities, *DA* and *DR*, respectively, which provide more direct measures of the microstructural dimensions (Fig. 2):

$$DA = \lambda_1 \tag{6}$$

$$DR = (\lambda_2 + \lambda_3)/2 \tag{7}$$

It has been shown in animal models that *DR* increases in WM with de- or dys-myelination (Song et al., 2002; Wu et al., 2011a). This observation appears to be consistent with

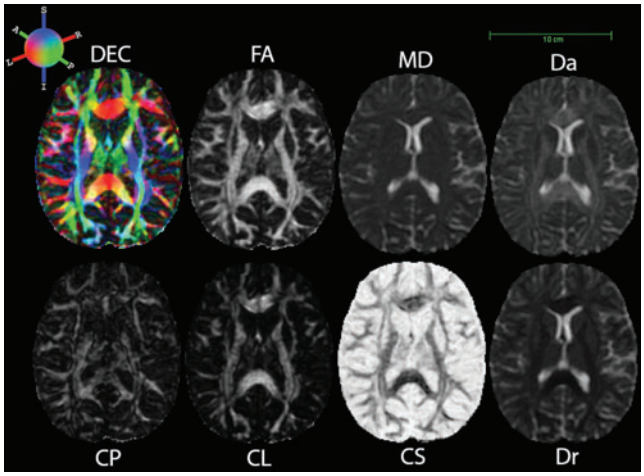

FIG. 2. Quantitative diffusion tensor imaging (DTI) stain maps from a single DTI data set.

many WM pathologies. Changes in the axonal diameters or density may also influence *DR*. The axial diffusivity, *DA*, tends to be more variable in a broad range of WM changes and pathology. In axonal injury *DA* decreases possibly due to the increased debris from the disrupted membrane barriers (Sun et al., 2006). The *DA*s of WM tracts have been reported to increase with brain maturation as well (Ashtari et al., 2007; Bava et al., 2010; Gao et al., 2009).

It is generally assumed that the major eigenvector, $\mathbf{e}_1$, direction is parallel to the orientation of the WM fiber bundles. A common representation of this directional information is to map the x, y, and z portions of the major eigenvector into red, green, and blue color channels, respectively, weighted by FA, which is referred to as the directionally encoded color (DEC) map (Pajevic and Pierpaoli, 1999) (Fig. 2). The DEC map representation is useful for identifying and mapping WM tracts relative to brain lesions before intraoperative mapping (Jellison et al., 2004; Witwer et al., 2002).

It is important to note that the interpretation of all DTI stains (other than *MD*) is particularly challenging in regions with significant partial volume averaging, particularly in areas of crossing WM tracts (Alexander et al., 2001; Wheeler-Kingshott and Cercignani, 2009). In these areas, the diffusion tensor does not truly characterize the distribution from multiple fiber populations and the diffusivities in the parallel and perpendicular directions. One simple strategy for identifying and characterizing fiber crossings is using the tensor shape, which may be broken down into prolate (linear) (*CL*), oblate (planar) (*CP*), and spherical (*CS*) components (Alexander et al., 2000; Westin et al., 2002) (Fig. 2):

$$CL = \frac{\lambda_1 - \lambda_2}{\lambda_1 + \lambda_2 + \lambda_3} \tag{8}$$

$$CP = \frac{2(\lambda_2 - \lambda_3)}{\lambda_1 + \lambda_2 + \lambda_3} \tag{9}$$

$$CS = \frac{3\lambda_3}{\lambda_1 + \lambda_2 + \lambda_3} \tag{10}$$

These shape stains, though not widely used, do provide a good assessment of where the diffusion tensor is most valid for describing WM properties—for example, where *CL* is highest (most prolate). Conversely, WM regions where either *CP* or *CS* is high will have problematic interpretations. Other strategies for describing shape properties of DTI include the skewness of the deviatoric portion of the diffusion tensor (Ennis and Kindlmann, 2006; Lange et al., 2010).

A major limitation of DTI is that it can resolve only a single fiber orientation within a voxel and fails in voxels with orientational heterogeneity (e.g., crossing fibers) (Alexander et al., 2001). This shortcoming stems from the tensor model's inherent assumption of Gaussian diffusion. The Gaussian function has only a single directional maximum, while voxels with multiple fiber orientations have multiple maxima, and hence cannot be described by a single Gaussian function. Consequently, such voxels will become partial volume averaged, with artificially reduced *FA* values, potentially precluding them from being as assigned as WM. Such failure poses a huge obstacle to WM tractography and interpretation of diffusion anisotropy (Pierpaoli et al., 2001).

The applications of DTI in the brain and spinal cord are rapidly expanding. It is currently the most widely used method for assessing WM changes in a broad range of brain diseases, injuries disorders, and changes with brain maturation, aging, and plasticity. A current PubMed search of DTI and brain or spine reveals more than 10,000 publications. Many of these applications and the interpretation of DTI measures are summarized in a recent review article (Alexander et al., 2007) and a recent book on diffusion MRI (Jones, 2011).

Beyond the diffusion tensor

The diffusion-weighted signal behavior at low levels of diffusion weighting (e.g., $b < 1500\,\mathrm{sec/mm^2}$) is fairly consistent with the diffusion tensor model. However, at higher levels of diffusion weighting (e.g., $b > 2000\,\mathrm{sec/mm^2}$), the signal decay is no longer observed to be mono-exponential (Clark and Le Bihan, 2000; Niendorf et al., 1996). Several studies (Mulkern et al., 1999) attributed this deviation from mono-Gaussian diffusion to apparent fast and slow diffusing components of the apparent diffusion coefficient, and measured the decay of the diffusion signal over a range of b-values to estimate the apparent fast and slow components. However, there is controversy over the assignment of these components and whether the bi-exponential model should take into account exchange between compartments (Mulkern et al., 1999).

Diffusion kurtosis imaging (DKI) (Jensen et al., 2005) is another technique that investigates the non-mono-Gaussian properties of water diffusion by measuring the kurtosis of the diffusion propagator, which could reveal brain microstructure information hidden to DTI. The scalar apparent kurtosis coefficient may be used to quantify the extent to which water diffusion in brain tissue is non-mono-Gaussian. More recently, the diffusion kurtosis (DK) tensor was developed to take into account the diffusion anisotropy (Lu et al., 2006). Similar to the diffusion tensor, the 3D kurtosis properties can be completely described by a tensor, in this case the DK tensor being a symmetric $3\times3\times3\times3$ matrix with 15 independent elements (compared to the 6 of the diffusion tensor). DKI differs from the bi-exponential model in that DKI does not make an assumption on the number or even existence of biophysical compartments. Analogous to the diffusion tensor, rotationally invariant scalar measures or stains can be obtained from the DK tensor, such as mean kurtosis (*MK*), axial kurtosis, and radial kurtosis. Recently, a growing body of literature has looked at how these measures relate to aging and pathology. In a study on the effects of aging on the human prefrontal cortex (Falangola et al., 2008), the authors reported increased GM *MK* with age, when moving from adolescence to adulthood. In a rodent brain maturation study (Cheung et al., 2009), the radial and axial kurtosis measures provided better detection and characterization of the developmental changes in various WM and GM structures than their DTI counterparts. Both studies reveal DKI's great potential to better characterize GM microstructure change, which can be difficult for DTI.

The clinical value of DKI has been validated in several studies that show its ability to detect tissue microstructure abnormality such as in human head and neck squamous cell carcinoma (Jansen et al., 2010), cerebral glioma (Raab et al., 2010), and lung dysfunction (Trampel et al., 2006). In a recently published study looking at DKI in a rat model of traumatic brain injury (Zhuo et al., 2012), the *MK* significantly

increased at the sub-acute stages of injury in all ipsilateral and contralateral regions, while standard DTI parameters gave inconsistent results. The authors associated the *MK* elevation with increased reactive astrogliosis, suggesting that DKI is sensitive to these microstructural changes, whereas DTI parameters alone may miss them. Although DKI is promising, it has not been studied or developed nearly as widely as DTI.

To resolve multiple fiber orientations, high angular resolution is needed, which can be achieved by increasing the *b*-value. In DTI, the *b*-value is typically $\sim 1000\,\mathrm{sec/mm^2}$, at which the angular resolution is poor for mapping crossing fibers. A growing number of high angular resolution strategies have been developed, based on increasing the number of encoding directions and in some cases multiple levels of diffusion weighting. In general, increasing the maximum diffusion weighting ($b > 2000\,\mathrm{sec/mm^2}$) up to $b \sim 17{,}000\,\mathrm{sec/mm^2}$ or more increases the ability to resolve fiber distributions with better angular resolution, to better characterize diffusion in complex tissue.

A general method for estimating the probability distribution of displacements or diffusion propagator is the *q*-space formalism (Callaghan, 1996; Cory and Garroway, 1990). The wave-vector $\mathbf{q} = \gamma \mathbf{G} \delta$ is analogous to the wave-vector $\mathbf{k}$ used in *k*-space sampling for MR image acquisitions. The diffusion signal in *q*-space and diffusion propagator are Fourier transform pairs:

$$P(\mathbf{R}, \Delta) = \int_{\mathbf{q} \in \Re^3} E(\mathbf{q}, \Delta) e^{-2\pi \mathbf{q} \cdot \mathbf{R}} d^3\mathbf{q}, \qquad (11)$$

where $P(\mathbf{R}, \Delta)$ is the diffusion propagator, which describes the displacement distribution of the water molecules within a diffusion time Δ. In DTI, the propagator is modeled as a 3D Gaussian distribution. Variations of *q*-space imaging have been implemented on clinical MRI scanners, despite violating the narrow gradient pulse requirement for *q*-space. Even with this violation, the Fourier relationship in Eq. (11) is a reasonable approximation (Bar-Shir et al., 2008; Mair et al., 2002; Wedeen et al., 2005), and the diffusion displacements are similar in shape to reality, but may be underestimated (Bar-Shir et al., 2008; Callaghan, 1996; Lori et al., 2003; Mair et al., 2002; Wedeen et al., 2005).

Diffusion propagator details may be estimated using a large number ($N_e > 40$ up to several hundred) of diffusion encoding directions with high angular resolution diffusion imaging (HARDI) strategies (Alexander et al., 2002; Frank, 2002; Tuch, 2004). HARDI acquisitions are on the order of 10–20 min or more at resolutions comparable to DTI studies. The most common application of HARDI studies is to estimate the orientation distribution function (ODF) of the diffusion propagator, which is a directional representation of the propagator (Tuch, 2004; Wedeen et al., 2005). Often these methods use a spherical harmonic model of the ODF. Spherical deconvolution of the propagator ODF with the expected single fiber group ODF may be used to estimate the fiber ODF, which is an estimate of the fiber orientations in a voxel (Tournier et al., 2004).

Strategies for combining high angular resolution and multiple levels of diffusion weighting include diffusion spectrum imaging (DSI) (Wedeen et al., 2005), hybrid diffusion imaging (HYDI) (Wu and Alexander, 2007), and combined hindered and restricted model of diffusion (CHARMED) (Assaf and Basser, 2005). The *q*-space sampling for DSI is on a Cartesian grid, while HYDI and CHARMED used measurements in spherical coordinates (shells of *q*-space). DSI and HYDI estimate the propagator by taking the Fourier Transform of the *q*-space signals as described in Eq. (11). These approaches require many measurements (>100 and up to 500 or more) at different levels of diffusion-weighting (up to $20{,}000\,\mathrm{sec/mm^2}$) and encoding angles. The acquisition time for whole-brain coverage with these approaches is on the order of 15 min to more than an hour. Recently, analytic model solutions for estimating the propagator based upon *q*-space measurements have been proposed, including diffusion propagator imaging (Descoteaux et al., 2011), spherical polar Fourier expansion (Assemlal et al., 2009), and Bessel Fourier orientation reconstruction (Hosseinbor et al., 2011). These analytic models may enable sparser sampling schemes of *q*-space to be used.

Other diffusion MRI measures

The HARDI and more general *q*-space sampling methods have resulted in other quantitative measures that may be used to characterize WM microstructure. A measure of the directional variation or anisotropy of the ODF is the generalized fractional anisotropy (*gFA*), which is analogous to the FA measure for DTI, but should maintain high anisotropy in areas of fiber crossing (Tuch, 2004). The *gFA* appears to be reduced in anterior thalamic radiations and cingulum tracts of patients with obsessive compulsive disorder (Chiu et al., 2011), reduced in the corpus callosum with increased alcohol use (Liu et al., 2010), and abnormally asymmetric in association WM tracts in autism (Lo et al., 2011).

A commonly used measure from DSI and HYDI is the zero-displacement probability, *Po*, which is the integral of the entire *q*-space signal, normalized by the $q = 0$ signal (Assaf and Cohen, 2000; Wu and Alexander, 2007). *Po* is the probability density of water molecules that minimally diffuse within the diffusion time and, hence, a measure of restricted diffusion. In a healthy adult brain, *Po* is greater in WM than GM because WM has more restricting barriers, including multilayer myelin sheaths, axonal membranes, and microtubules. It also appears to be insensitive to WM fiber crossings, which cause reductions in the *FA* of DTI. Another measure of the propagator is the mean squared displacement (*MSD*), which is a displacement variance measure of the diffusion propagator; however, it is very sensitive to the measurement noise (Assaf and Cohen, 2000; Wu and Alexander, 2007). The *MSD* may be used to estimate the apparent diffusion coefficient by MSD/Δ. Another measure of diffusivity from DSI and HYDI is the *q*-space inverse variance (*QIV*), which is the inverse of variance of the *q*-space signal distribution (Wu et al., 2008). Note that for Gaussian diffusion, the *QIV* is the *MSD*, but is only an approximation in the case of non-Gaussian diffusion. Example quantitative *q*-space stain maps are shown in Figure 3.

Several studies have looked at age-related changes in *Po* of WM. In healthy children, *Po* was found to increase with brain maturation, but then plateau during adolescence (Ben Bashat et al., 2005). This age-related plateau was also observed in an *in vivo* HYDI canine study (Wu et al., 2011a) of brain maturation, where *Po* of global WM was computed in control dogs within the age range 3–16 months (similar to the period of

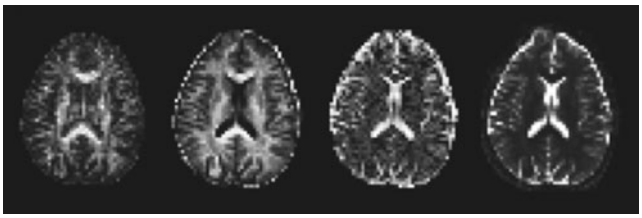

FIG. 3. Diffusion magnetic resonance imaging (MRI) stains from the same hybrid diffusion imaging study and slice–fractional anisotropy (*FA*), zero-displacement probability (*Po*), mean-squared displacement (*MSD*), and *q*-space inverse variance (*QIV*). Note the higher apparent noise and heterogeneity in the MSD map in comparison to the QIV.

early childhood through adolescence in humans). In another HYDI study (Wu et al., 2011b) on age-related changes in cerebral diffusion properties in healthy adult human brains, *Po* was found to be relatively constant across the age range (18–72 years). Several studies have shown *Po* to be sensitive to brain pathology. In a high *b*-value study of multiple sclerosis (MS) (Assaf et al., 2002), *Po* was reduced in both lesions and normal appearing white matter (NAWM). A recent *in vivo* HYDI study (Wu et al., 2011a) in a canine model of dysmyelination showed a significant reduction in the *Po* of WM in sick dogs with respect to controls, which is consistent with previous high *b*-value measurements in fixed, postmortem spinal cord and brain specimens from myelin deficient rats (Bar-Shir et al., 2009; Biton et al., 2007). These studies suggest that changes in myelin are a significant mechanism for the differences in *Po*, though the axonal density and diameter may also play a role in modulation of *Po*.

Tractography

In DTI, it is generally assumed that the major eigenvector is parallel to the local WM fiber orientation. Newer methods with many encoding directions (e.g., HARDI as discussed above) can estimate the directions of multiple fiber bundles. Tractography is a method for reconstructing the trajectories of major WM tract pathways using the orientation information from DWI. These methods can create 3D depictions of WM tracts (e.g., see Fig. 4).

At the foundation for many tractography methods is the streamline algorithm (Basser et al., 2000; Conturo et al., 1999; Mori et al., 1999), which estimates the WM trajectories in a propagation vector field. The most commonly used propagation vector is the major eigenvector from DTI, but one or multiple propagation vectors for each vector may be derived using the ODF from either HARDI or DSI. The simplest version of this is to step through the vector field in the direction of the local vector for small, finite distances. Smoother reconstructions may be obtained using higher order Runge-Kutta spatial integration methods.

The streamline algorithm is the basis for both deterministic and probabilistic tractography approaches. In deterministic tractography, a single reconstruction is produced for a given DTI data set. Probabilistic tractography methods attempt to characterize the uncertainty in the tract reconstruction, by performing a Monte Carlo tractography experiment by repeating the streamline reconstruction multiple times and perturbing the propagation vector field for every iteration (Lazar and Alexander, 2005; Parker et al., 2003). Strategies for this perturbation include adding noise to the tensor field or bootstrap resampling of the DWI data. In general, the dispersion of the reconstructed tracts increases with the distance from the starting location and decreases with increased diffusion anisotropy (Anderson, 2001; Lazar and Alexander, 2003; Lori et al., 2002).

An alternative strategy for reconstructing WM tracts is global tractography that attempts to find a reconstruction solution that is most consistent with the underlying diffusion MRI data. Global tractography methods include (1) constraining the connection endpoints (Cheng et al., 2006) and (2) optimizing a synthesized diffusion tensor field based upon tractography reconstruction (Fillard et al., 2009; Kreher et al., 2008). The latter approaches are very computationally demanding.

Recently, an interesting strategy for tractography reconstruction is to reconstruct the pathways on much smaller voxels, which reveals tract details that are much finer than the original resolution. Reconstructing the tracts on voxel grids

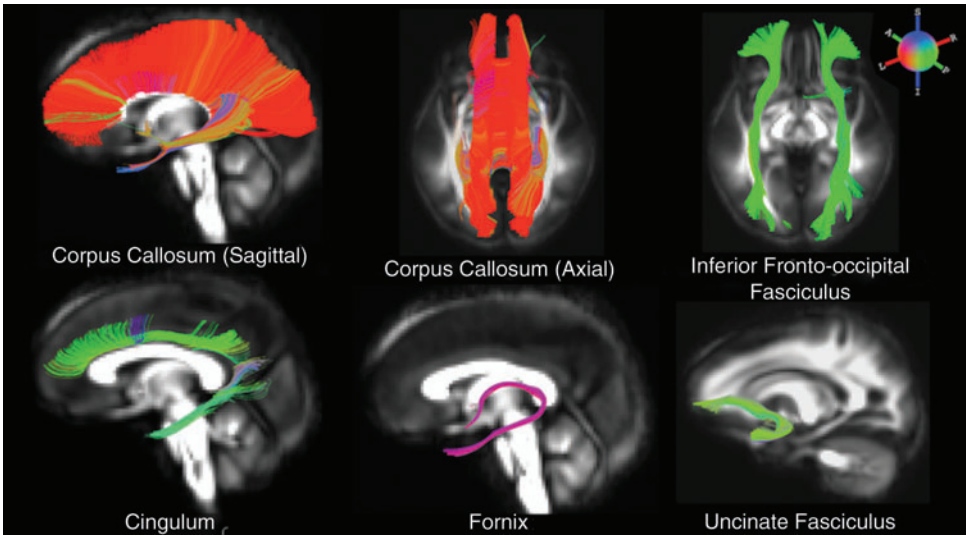

FIG. 4. White matter (WM) tract reconstructions for several major WM pathways.

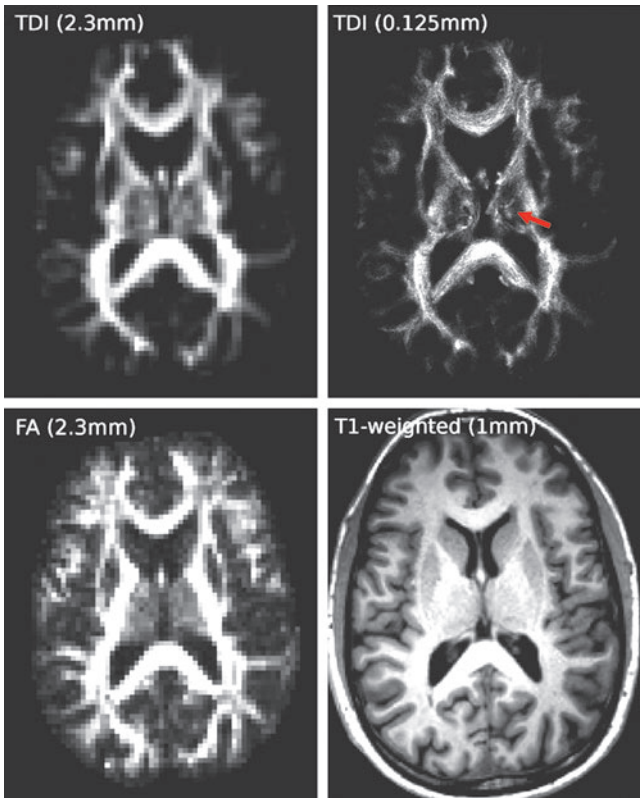

FIG. 5. Top row: track-density imaging (TDI) examples without super-resolution (left) at the native resolution of the acquired diffusion MRI data (2.3 mm isotropic) and with super-resolution (right) using a grid-size of 125 μm. Note: the same diffusion MRI data and whole-brain tracking dataset (with 2.5 million tracks) were used to create both images; the only difference was the grid-size used to calculate the TDI map. The sub-voxel detail achievable with super-resolution is readily seen. For comparison, the bottom row shows the FA map generated from the same diffusion MRI data used to create the TDI maps, and an anatomical high-resolution three-dimensional (3D) T1-weighted image (1 mm isotropic resolution). The super-resolution TDI map shows not only sub-voxel detail but also novel image contrast (e.g., see high contrast within the thalamus [arrow] and in the optic radiations). Image courtesy F. Calamante.

with dimensions an order of magnitude smaller than the original acquisition appears to have super-resolution properties that may provide a unique image contrast mechanism (Calamante et al., 2010). The concentration or density of tracts is potentially a unique contrast mechanism (Calamante et al., 2010, 2012; Roberts et al., 2005), though caution should be used for interpreting as a quantitative measure. Superrresolution tractography is promising for mapping very fine WM detail below the original spatial resolution of the DTI data (e.g., the thalamus in Fig. 5). The extended coherence of the tractography pathway reconstruction can significantly constrain the WM detail at subvoxel levels. This superresolution property is also manifest by differences in the reconstructed pathways for multiple subvoxel seed points within a voxel. Pure upsampling of the DTI data merely provides a smoother image and does not yield similar hyperfine detail.

The main applications for tractography are (1) stains for visualization of specific WM tracts, (2) defining regions-of-interest (ROIs) for quantitative analyses, and (3), more recently, characterizing connectivity properties between two or more brain regions. The visualization of tractography maps may be used to generate virtual dissections of brain anatomy (e.g., Fig. 4). A clinical application of tractography is to visualize the location of WM tracts relative to a lesion or within a region of planned surgical intervention (Witwer et al., 2002). The application of tractography for quantitative image analysis is described further in the section on analysis methods.

Finally, an exciting application of this technology is to generate connectomes of structural connectivity in the brain (Hagmann et al., 2007, 2008). Structural connectomes may be generated using whole-brain tractography to assess the presence, absence or strength of connections between two or more brain regions. This approach permits the comparison of structural connectivity against functional connectivity defined by fMRI (Honey et al., 2007) or electrophysiology (Sporns et al., 2005). A connectome is a descriptive mathematical construct (e.g., an association matrix) where "edges" describe the connectivity or interactions between nodes of the connectivity graph. The most common way for generating a structural connectomes graph is to define the nodes by parcellation of the cortex and subcortical areas. Two nodes may be considered connected if tractography yields a reconstructed connection between the two nodes. A connectivity graph or associate matrix may be generated using the end-point or cortical regions as nodes and the tractography counts as the edges (Hagmann et al., 2007). Edge weights of the graphs may be defined as the tract connection count, or a binary threshold (Hagmann et al., 2007). Another possibility for edge weights is to integrate the *FA* or some other qMRI measure along the tract pathways. Analyses of the association matrices may yield measures and properties of graph connectivity including small-worldness, efficiency, hubs, distance, and clustering coefficients (Bassett et al., 2011; Gong et al., 2009; Hagmann et al., 2007). Several excellent articles discuss methods and measures for characterizing and representing brain connectivity properties based upon structural connectomes (Hagmann et al., 2010; Rubinov and Sporns, 2010). DSI appears to yield more accurate and robust connectivity properties than DTI (Bassett et al., 2011). Further, the connectivity properties appear to be relatively stable within subject yet are sensitive to differences between individuals (Bassett et al., 2011). Structural connectome properties have been investigated in several population based studies. One study investigated connectivity properties as a function of age and gender in adults (ages 19–85 years) and found reduced connectivity properties with age and in men (Gong et al., 2009). Conversely, the connectivity properties increase with age in children (Hagmann et al., 2010). Decreased structural connectivity has been observed in patients with Alzheimer's disease (Lo et al., 2010).

One of the key challenges in defining structural connectomes is the definition of node regions in the brain. Recently, a data-driven method, known as epsilon radial connectomes, was proposed by Adluru et al. (2012) and Chung et al. (2011b). A sample illustration of the technique using DTI data is shown in Figure 6. The main idea is to define node regions using clustering tracts in spatially normalized DTI data. In the particular framework (Adluru et al., 2012; Chung et al., 2011b), the authors identify nodes by clustering tract end

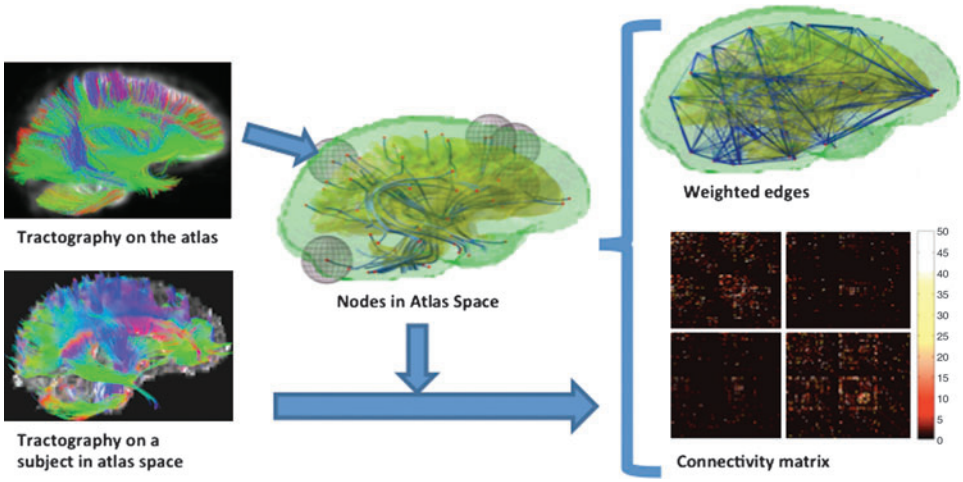

FIG. 6. Construction of a structural connectivity matrix (connectome) based upon diffusion-weighted imaging tractography with epsilon-radial nodes. Tractography is performed in normalized space. Nodes are generated using spherical nodes based upon clusters of tract terminations. Tract-counts are used to generate the connectivity matrix.

points into spherical volumes of a particular radius (typically the amount of smoothing used in voxel-based analyses, e.g., 8 mm). One can extend the framework to identify nodes by clustering the tracts based on their shape instead of just using end points.

There are several significant caveats and limitations with tractography. A major one is that the tract reconstructions are highly sensitive to errors anywhere along the pathway (Lazar and Alexander, 2003). An artifact in a single plane can lead to highly aberrant pathways (Pierpaoli et al., 2001). In general, tractography algorithms are poor at resolving crossing fibers (Barrick and Clark, 2004). Even tractography reconstructions that include HARDI measurements of crossing fibers may not necessarily reflect the actual connection strengths through these regions. Tractography methods are prone to both false positives (erroneous tracts) and false negatives (missing tracts), which can make the interpretation of tractography measurements challenging (Jones, 2011; Pierpaoli et al., 2001). In particular, the application of tractography to neurosurgical planning should be handled with care (Kinoshita et al., 2005). It should be noted that the interpretation of tractography can be challenging as even erroneous tract reconstructions often appear realistic. Expanded descriptions of tractography methods may be found in recent review articles (Chung et al., 2011a; Lazar, 2010) and book chapters 22–24 in Jones (2011).

Tracer Imaging of Brain Connections

Despite the recent proliferation of WM tractography studies and applications, it is difficult to assess whether a reconstruction is reflecting reality. The reasons for this are elaborated above. Several studies have evaluated tractography algorithm performance using anisotropic diffusion phantoms (Moussavi-Biugui et al., 2011; Perrin et al., 2005; Poupon et al., 2008; Watanabe et al., 2006) and synthetic phantom data (Close et al., 2009; Fillard et al., 2011; Lazar and Alexander, 2003). While these tools are good for investigating the properties of tractography algorithms, they may not adequately and realistically mimic the errors associated with neuroimaging and the complexity of WM in the brain. The most standard approach for validation is to compare the connected regions to the tract definitions from classic axon tracer and dissection studies (Caspers et al., 2011; Dauguet et al., 2007; Kier et al., 2004a, 2004b; Lawes et al., 2008; Schmahmann et al., 2007). Another promising approach for tracing WM pathways *in vivo* is using manganese, which is taken up by the calcium channels of the axons (Lin et al., 2001; Yamada et al., 2008). Using manganese, it is possible to trace transynaptic connections across distant brain regions. Manganese is paramagnetic which reduces the T1 of the tissue, leading to focal tissue enhancement of the specific pathways. In high enough doses, manganese is toxic to neurons though many research studies have applied it in living animal systems. To date, it has been used to map out the trajectories of the optic nerves, projections from the putamen and caudate in nonhuman primates, and from cortical regions (Murayama et al., 2006; Saleem et al., 2002). A recent study compared manganese tracer results with DWI tractography in minipigs, which showed fairly good (but not identical) correspondence (Dyrby et al., 2007).

MT Imaging

It would be ideal to be able to directly image myelin in WM directly. Unfortunately, the 1H protons of myelin are essentially invisible using traditional MRI. The protons bound in myelin proteins and lipid bilayers have extremely short transverse relaxation times ($T2$s), which are in the microsecond range compared to the millisecond range of free water. However, dipolar coupling and chemical exchange facilitates an exchange of magnetization between two pools of protons—a free pool (e.g., water) and a bound pool (e.g., myelin macromolecules) (Fig. 7). This mechanism is known as MT (Wolff and Balaban, 1989), which may be used to sensitize MRI-visible water signal to the myelin macromolecular content. One way to induce the MT effect is to apply a strong off-resonance RF pulse at a frequency far from the free water resonance frequency (>1000 Hz). The MT saturation pulse selectively saturates the magnetization of macromolecule-bound protons, which have a very broad frequency spectrum (the bandwidth is inversely proportional to $T2$), while leaving the free pool (long $T2$ with a narrow spectrum) relatively unaffected. Subsequently, the fast exchange of magnetization between the pools will partially saturate MRI-visible free water protons causing a decrease of the observed MRI signal intensity (Fig. 8). The MT attenuation of the free water signal is a complex function of the MT pulse properties (amplitude, rate, and frequency offset), the concentration of

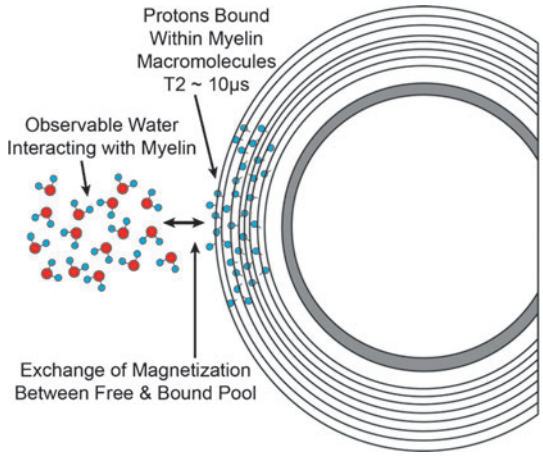

FIG. 7. Schematic illustration of magnetization exchange that is detected by magnetization transfer imaging methods.

macromolecules, and the exchange rate of the magnetization between the free water and bound macromolecular pools. The MT effect is modulated by the offset frequency and amplitude of the RF saturation pulse. Maps of MT stains or measures are generated through weighted combinations (filters) of the saturation-weighted images at different frequencies and pulse amplitudes, discussed below.

MT ratio

The most common stain for characterizing the MT effect is the MT ratio (*MTR*), calculated as the relative change in intensity of images acquired without (S_o) and with (S_{MT}) off-resonance MT pulses:

$$MTR = \frac{S_o - S_{MT}}{S_o} \tag{12}$$

The example source images and corresponding *MTR* map are shown in Figure 9.

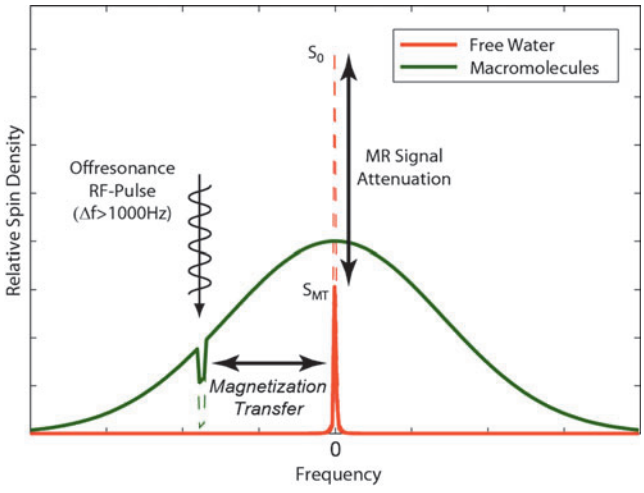

FIG. 8. Schematic of the magnetization transfer (MT) saturation process. An intense refocusing (RF) pulse is applied off-resonance, which saturates the magnetization of the macromolecule pool. Rapid exchange between magnetization of the macromolecule proton pool and the free water protons nearby attenuates the free water signal.

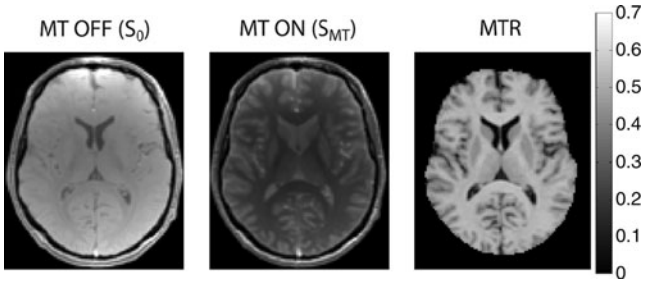

FIG. 9. Example images from an MT ratio (*MTR*) experiment. The image obtained without any MT saturation (left) shows little contrast between WM and gray matter (GM). Additional application of MT pulse (18-ms Fermi pulse, offset 2.5 kHz, MT flip 1100°, repetition time [TR] = 40 msec) causes strong reduction of MR signal in tissues with natural abundance of myelin such as WM (middle), which in turn results in higher values in the corresponding *MTR* (right).

Increased *MTR* values are most often associated with increased macromolecular concentrations in the tissue. The higher *MTR* in WM is believed to be associated with the proteins and lipids associated with myelinated axons (Stanisz et al., 1999). Consequently, the *MTR* in WM is reduced in demyelinating diseases such as MS although the *MTR* can also be influenced by overall water content and other macromolecules in processes such as neuroinflammation (Stanisz et al., 2004). The reported ranges of *MTR* values in healthy WM and GM are roughly 0.4–0.55 and 0.25–0.3, respectively. This wide range in *MTR* values reflects the variability of *MTR* measurements across scanners, transceiver coils, and scanned objects (Berry et al., 1999; Filippi et al., 2000; Silver et al., 1999). One source of variability of *MTR* in the literature is a lack of standardization of pulse sequence protocols. In each particular implementation, the exact *MTR* measurement will depend upon the pulse sequence parameters (e.g., TR, TE, and excitation flip angle), the magnetic field strength, as well as the shape, amplitude, and frequency offset of the saturation pulses. Consequently, within a single *MTR* study, the imaging parameters should be fixed to maximize consistency. Efforts have been also made to solve the stability issues (Tofts et al., 2006) and standardize *MTR* studies across multiple sites. Another major source of *MTR* variability (especially at magnetic field strengths of 3T and higher) is system-specific and object-specific inhomogeneity of the B1 excitation field and the main B0 field. B0 inhomogeneities are caused by incomplete shimming and spatial variations in the magnetic susceptibilities in soft tissue, bone, and air, which lead to shifts (errors) in the saturation frequency offsets. At high magnetic fields (B0 > 1.5T), inhomogeneities in the B1 field may reach up to ±30% within the imaged object and will affect the saturation pulse amplitude and consequently alter the level of MT saturation. The B1 field may be measured and used to retrospectively correct *MTR* measurements (Ropele et al., 2005; Samson et al., 2006; Yarnykh, 2009). Figure 10 demonstrates the effect of B1 field correction (Yarnykh, 2009). Unlike correction of receiver coil inhomogeneity, correction of B1 transmit field effects on *MTR* is not trivial due to its effect on MT power deposition and effect on the excitation flip angle. Full correction of B1 effects is only possible using the more complete description of MT effect (such as provided by two-pool model in the next section). B1

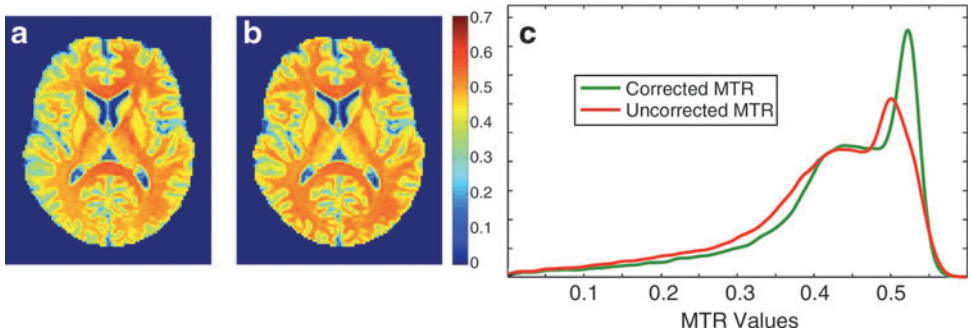

FIG. 10. Effect of B1 inhomogeneity on *MTR*. Uncorrected *MTR* map **(a)** demonstrates by slow spatially varying intensity inhomogeneity **(a)**. Correction of *MTR* using separately acquired B1 map eliminates the intensity bias **(b)** and leads to improved localization of WM and GM peaks on the corresponding whole brain histograms **(c)**.

correction of *MTR* relies on some approximations to the model. Other considerations for *MTR* measurements are discussed in two excellent review articles (Henkelman et al., 2001; Horsfield et al., 2003).

Quantitative MT imaging

As discussed above, the *MTR* measurement is highly dependent upon a broad range of technical factors. Moreover, despite its sensitivity to macromolecular tissue content, the traditional *MTR* is a nonspecific indicator of underlying pathology that is affected by free water MR parameters (Tofts, 2003), which are modulated by other factors, for example, by inflammation (Stanisz et al., 2004). Fully quantitative MT (qMT) methods are required to improve the sensitivity, specificity, and stability of MT metrics (Gochberg et al., 1999; Gochberg and Gore, 2003; Ropele et al., 2003). Several investigators have adapted a two-pool model of MT for *in vivo* measurements (Sled and Pike, 2001; Tozer et al., 2003; Yarnykh, 2002, 2004; Yarnykh and Yuan, 2004). The two-pool model is fitted to data acquired with MT pulses over a range of offset frequencies and pulse amplitudes to estimate several underlying physical parameters of the tissues; most important are bound pool fraction (*BPF* or *f*) (relative concentration of macromolecules), cross-relaxation rate (*k*), the *T2b* and *T2f* (the relaxation times of the bound and free pools, respectively), and longitudinal relaxation rate of the free pool *R1*. The advanced qMT imaging (qMTI) protocols also include separate acquisitions of B1 and B0 maps, which are used in the data fit to mitigate the impact of scanning imperfections on the quantitative maps (Yarnykh, 2007). Example quantitative maps estimated using a modified cross-relaxation imaging method (Mossahebi and Samsonov, 2011; Yarnykh, 2004; Yarnykh and Yuan, 2004) are shown in Figure 11. Several studies confirmed that qMT methods are much more sensitive and specific to macromolecular content than the conventional *MTR* methods (Dula et al., 2010; Schmierer et al., 2007; Tozer et al., 2005). Current implementations of qMTI can achieve spatial resolutions on the order of 1.5–2 mm; however, the scan times remain long (30 min or more).

Applications of MTI stains

MTI is emerging as an advanced MRI method sensitive to various CNS injuries (Filippi and Rocca, 2004). Many of the published MT studies have focused on patients with MS, who show decreased MT in both ROI and whole-brain histogram analyses. There is growing evidence that MT-based MRI may be the most sensitive imaging technique capable of tracking myelin changes in patients with MS (Chen et al., 2005, 2007; Deloire-Grassin et al., 2000; Dousset et al., 1992, 1995; Schmierer et al., 2004; Trapp et al., 1998). MT contrast is a stronger predictor of MS disease course than conventional MRI measures (Pike et al., 2000; Rovaris et al., 2003; Santos et al., 2002). In other diseases, similar results were obtained, indicating that *MTR* is a viable marker for affected white and GM. *MTR* has been shown to increase with brain development during the first several years of life (Rademacher et al., 1999; van Buchem et al., 2001) and regional decreases with aging have been found (Armstrong et al., 2004). Differences in *MTR* were sufficiently large to distinguish patients with mild cognitive impairment from patients with Alzheimer's disease and controls (Kabani et al., 2002a, 2002b). A number of published studies have also used MT methods to compare the brains in patients with schizophrenia against healthy control subjects (Bagary et al., 2003; Foong et al., 2001; Kiefer et al., 2004; Kubicki et al., 2005). Reduced *MTR* measurements in corpus callosum and occipital WM have also been observed in a small sample of patients with late-life major depressive disorders (Kumar et al., 2004).

Several studies have revealed potential clinical significance of qMT measures. The qMT measures were sensitive to tissue

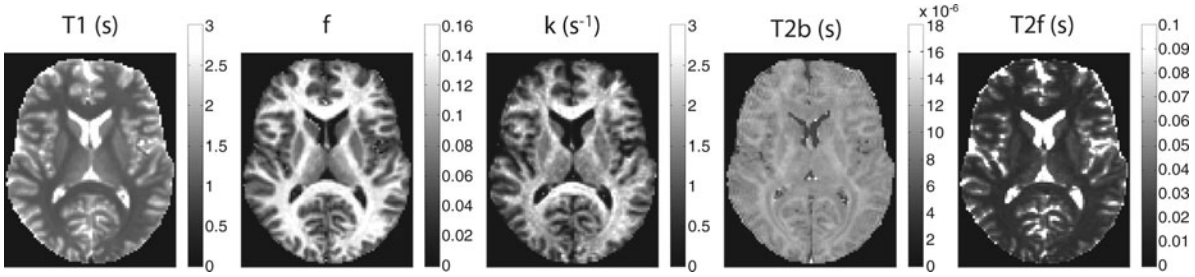

FIG. 11. Quantitative maps or stains of MT effect obtained in a healthy volunteer.

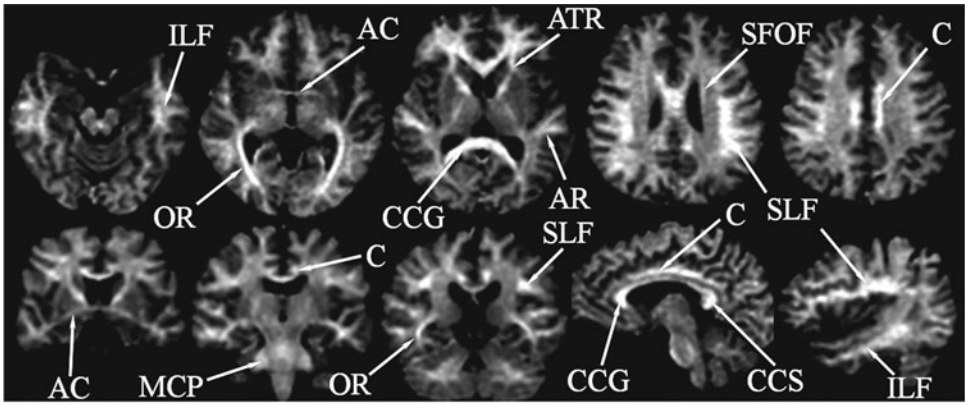

FIG. 12. Anatomy of major fiber tracts on 3D bound pool fraction maps produced by constrained cross-relaxation imaging. The following anatomic structures are labeled: ILF, inferior longitudinal fasciculus; OR, optic radiations; AC, anterior commissure; CCG, corpus callosum genu; CCS-corpus callosum splenium; AR, auditory radiations; ATR, anterior thalamic radiations; SLF, superior longitudinal fasciculus; SFOF, superior fronto-occipital fasciculus; C, cingulum; MCP, middle cerebellar peduncle. Courtesy of Dr. Vasily Yarnykh. Figure reproduced from Yarnykh and Yuan (2004), with permission from Elsevier.

composition manifested as regional variations in WM of the brain (Sled and Pike, 2001). Anatomical correlations of qMT parameters estimated by constrained cross-relaxation imaging (Yarnykh, 2004; Yarnykh and Yuan, 2004) also revealed the increase of *BPF* in major fiber tracts of the human brain (Yarnykh, 2004; Yarnykh and Yuan, 2004) and rat brain (Underhill et al., 2011), showing the strong association of *BPF* with the fiber density (Fig. 12). The *BPF* was able to track myelin levels in MS lesions (Davies et al., 2004).

A few studies have attempted to relate MT measurements to measures reflecting brain function. A serial *MTR* study in the optic nerves of 29 patients with acute optic neuritis was performed with measurements of visual system functioning using visual evoked potentials (VEP) (Hickman et al., 2004). No significant differences in *MTR* were observed between patients and controls at the onset of optic neuritis, although the *MTR* did decrease in patients over a period of 1 year. There did not seem to be any direct relationship between *MTR* and VEP measurements. Another study of 18 patients with early-stage MS (Au Duong et al., 2005) demonstrated a correlation between functional connectivity between left Brodmann areas 45/46 and 24 using an fMRI working memory task, and the *MTR* of NAWM and also with brain *T2* lesion load. Consequently, the functional connectivity relationship with *MTR* suggests that changes in the functional working memory network is related to changes in the WM pathophysiology. The *MTR* in normal appearing brain tissue (NABT) has a stronger correlation with cognitive impairment in MS patients than MS lesion load (Filippi et al., 2000). Whole-brain *MTR* histograms have correlated with neuropsychological impairment in MS patients (Rovaris et al., 1998; van Buchem et al., 1998). A combined *MTR* and fMRI study (Filippi et al., 2002) of simple motor function in patients with MS revealed correlations between the *MTR* histogram features of whole-brain, NABT (both GM and WM), and fMRI signal strengths in ipsilateral sensorimotor cortex and supplementary motor area (bilaterally). The fMRI signal in the contralateral sensorimotor cortex was significantly correlated with *MTR* histogram features in patients with cervical but not dorsal spinal cord myelitis (Rocca et al., 2006). A recent combined *MTR* and DTI study of 40 schizophrenia patients and 40 healthy participants showed decreased *FA* in the left uncinate fasciculus in the patients with longer illness duration and increased mean *MTR* in the right uncinate fasciculus (Mandl et al., 2010). Finally, an interesting study comparing *MTR* and *FA* of fronto-striatal WM pathways in attention deficit/hyperactivity disorder (ADHD) showed reductions in *FA*, but not in *MTR*, suggesting that the microstructural features are more altered than myelin in ADHD (de Zeeuw et al., 2011).

The remaining challenges of *MTR* imaging to serve as a stable and reproducible measure of neural tissue integrity include standardization of *MTR* protocols and making *MTR* imaging independent of system- and object-specific factors. Recently, an alternative MT measure, MT saturation, was proposed to minimize variability related to B1 effects (Helms et al., 2008). In this approach, MT measurements are augmented with an additional T1w scan, which is used along with MT-weighted data to yield MT saturation maps. Truly, qMTI has the potential to overcome aforementioned shortcomings of *MTR*. Unfortunately, no studies to date have attempted to relate qMT measures to brain function. One possible reason is a limited clinical utility of early qMT methods, which incurred a multiple fold increase in scan time (>1 h) compared with *MTR*. Recent developments demonstrated that optimized acquisition is possible within clinically acceptable times (Cercignani and Alexander, 2006; Underhill et al., 2009), which may facilitate application of these sensitive methods in clinical studies.

Relaxometry

Physical mechanisms

The signal intensity of different brain tissues in a typical MRI experiment is a function of the fundamental properties of water protons within the tissue. The interaction of the surrounding tissue environment with water protons influences the relaxation times of both the longitudinal and the transverse components of the magnetization. These interactions are influenced by the random motion (e.g., diffusion) and local magnetic field fluctuations within the tissue medium.

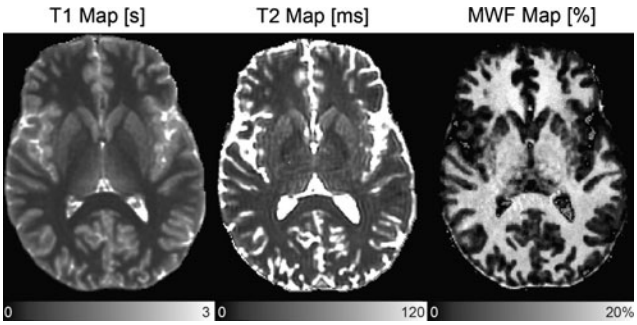

FIG. 13. Examples of typical steady-state relaxometry maps acquired at 2 mm isotropic resolution: left, T1; middle, T2; right, myelin water fraction (MWF).

The spin-lattice relaxation time (*T1*) is the recovery of longitudinal magnetization back to equilibrium after excitation by a radiofrequency pulse. The spin-spin relaxation time (*T2*) is the decay time associated with the loss of transverse magnetization signal due to dephasing. Additional dephasing due to reversible field gradients (*T2'*) leads to a more rapid loss of signal ($T2^* < T2$) when a 180° RF pulse is not utilized. In addition to relaxation, the strength of the observed signal is also a function of the overall proton density (*PD*), or number of nuclei contributing signal within a given voxel. In general, more restricted, dense or viscous tissue environments will exhibit reduced *T1* and *T2*. The presence of metal ions in the tissue will also influence the relaxation properties. Example *T1* and *T2* maps are shown in Figure 13.

By exciting and acquiring MR signal at different time intervals or sequence filters (i.e., TR and TE), one may preferentially stain the intensity and contrast of different tissues, generating *T1*-weighted (*T1*w), *T2*w, or *PD*w anatomical images. Relaxometry, on the other hand, refers to quantitative methods to map relaxation times within tissues. Accurate techniques seek highly specific measurements of one particular parameter (*T1*, *T2*, or *PD*), and thus remove other confounds to image contrast such as receiver coil sensitivity profiles or *PD* (in the case of *T1* and *T2*; see Fig. 13). These images show improved contrast between brain structures (Deoni et al., 2005a, 2005b) and may be more useful for the segmentation of brain tissue types than traditional imaging (Alfano et al., 1997). In the context of brain connectivity, these maps may provide more specific delineation of brain structures to serve as priors or landmarks for structural connectivity methods such as tractography.

T1 and *T2* are sensitive measures of the local microstructural environment within WM tracts. Although many studies show that neurological diseases affect *T1* and *T2*, these relaxation times depend on a wide range of tissue factors and are thus nonspecific. Both are highly dependent on water content, and tend to increase with bulk water in tissues. *T1* may also decrease with decreasing lipid content, as observed in MS plaques (Lacomis and Osbakken, 1986), while *T2* decreases as the size of the local water compartment becomes restricted.

Traditional methods

Traditional gold-standard methods to measure *T1* rely on saturating or inverting the longitudinal magnetization, sampling its recovery at different time points (TI) (Pykett et al., 1983), and then fitting it to a monoexponential model of magnetization recovery. This method is slow, as it requires multiple inversion times and a TR approximately five times longer than *T1* to allow complete recovery of longitudinal magnetization. Although the Look–Locker method (Look and Locker, 1970) improves the efficiency of the technique by sampling multiple TI per repetition, all inversion techniques are limited in spatial resolution due to long scan times.

Traditional methods to measure *T2* rely on obtaining spin echo measurements at different TEs and fitting them to a monoexponential model of signal decay. *T2** measurements are similar to *T2*, except a 180° RF pulse is not used. Multiple spin echoes can be measured in each repetition with the Carr-Purcell-Meiboom-Gill (CPMG) method (Meiboom and Gill, 1958). However, this sequence is extremely sensitive to imperfect RF pulses, which will generate magnetization that follows a *T1* pathway and thus overestimates *T2*. These can be suppressed with a proper sequence of crusher gradients inserted symmetrically around RF pulses (Look and Locker, 1970).

Rapid methods

Faster methods of relaxometry rely on steady-state acquisitions. The variable flip angle method (Christensen et al., 1974), also known as DESPOT1 (Homer and Beevers, 1985), can generate a *T1* map from spoiled gradient echo (SPGR/FLASH) images at two or more flip angles, while the DESPOT2 method can generate a *T2* map from steady-state free precession (bSSFP/FISP/FIESTA) at two or more flip angles in combination with DESPOT1 *T1* maps (Deoni et al., 2003). These techniques may be more attractive in the context of brain connectivity, as whole-brain coverage can be achieved at high resolutions and reasonable scan times (Deoni et al., 2005b). These methods are also extremely easy to optimize given a single *T1* time (Deoni et al., 2005b) or a range of expected *T1* values (Cheng and Wright, 2006), and can be casted into a linear form for straightforward data fitting. The estimation of *T2* from steady state sequences is a bit more complex as the signal also depends upon *T1*, so that both must be measured in the same experiment.

Although steady-state techniques have clear advantages over traditional relaxometry, they must be implemented carefully to ensure accurate measurements. Both DESPOT1 and DESPOT2 suffer from a strong dependence on excitation flip angle, although several well-matched steady-state calibration techniques have been developed to correct for this (Deoni, 2007; Sacolick et al., 2010; Yarnykh, 2007). DESPOT1 is also highly sensitive to proper SPGR sequence spoiling (Yarnykh, 2010), which may require the use of large gradients and increase the overall time of the technique. DESPOT2 also suffers from a strong dependence on main field inhomogeneity; a technique to correct this has been developed, although it requires twice as many data points to be acquired (Deoni, 2009). Even with careful consideration to these technical issues, further errors may be present due to an incomplete model of the MR signal. In addition to *T1* and *T2* relaxation, the rapid radiofrequency excitation of steady-state sequences may induce on-resonant MT effects, biasing *T1* measurements based on the macromolecular content of tissues (Ou and Gochberg, 2008). A typical DESPOT1 protocol at 3T involves two SPGR scans and a flip angle calibration scan

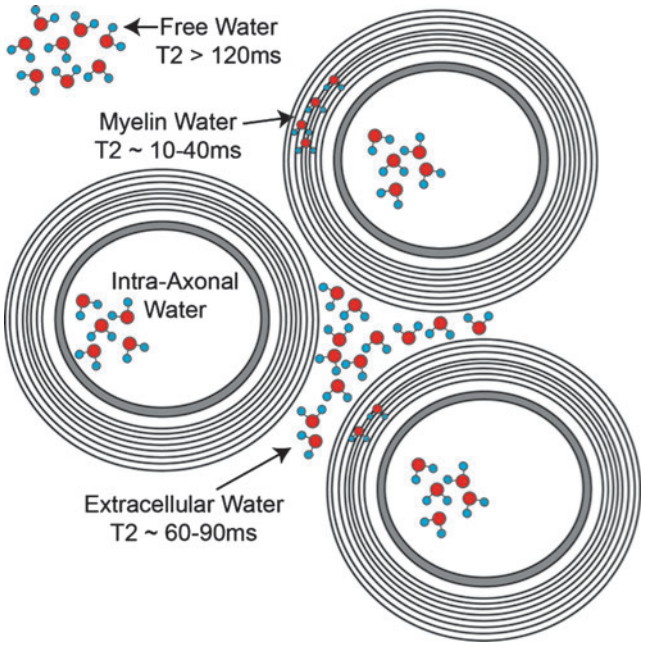

FIG. 14. Schematic illustration of different water environments within WM. Geometrically restricted compartments exhibit a much shorter *T2* due to restricted degrees of translational and rotational freedom.

(usually performed at ½ resolution, as this parameter is spatially smooth). A typical 1.5-mm isotropic resolution protocol with AFI flip angle correction (Yarnykh, 2007) takes about 10 min. Resolution can be increased at the cost of longer scan time, but is not limited by gradient performance or distortions as in EPI acquisitions typically utilized in diffusion imaging. For example, excellent results at 0.34 mm^3 isotropic resolution have been achieved through multiple averaging of DESPOT1 datasets (Deoni et al., 2005a).

Multicomponent relaxometry

All of the aforementioned relaxometry methods, both traditional and steady-state, operate under the assumption of a single, well-mixed pool of water within each voxel. This is an inaccurate assumption in the case of neural tissues, as water is known to exist within extracellular, intra-axonal, and myelin spaces separated by diffusion barriers. In particular, the water that is trapped in the myelin bilayers has extremely limited mobility, which significantly reduces the *T2* of myelin water (Fig. 14). In the case of CPMG *T2* imaging, this results in a nonmonoexponential decay of the signal with TE (MacKay et al., 1994; Menon and Allen, 1991; Whittall et al., 1997). This has led to the development of multicomponent *T2* (MET2) relaxometry, which seeks to model multiple *T2* values in distinct components of water within a single voxel, such as free water (e.g., edema and CSF, which have long $T2 > 120$ msec), extracellular water ($T2 \sim 60$–90 msec), and water within the myelin membranes of axons ($T2 \sim 10$–40 msec) (MacKay et al., 1994; Stewart et al., 1993). The ratio of the myelin water component to the overall signal has been coined myelin water fraction (*MWF*) (Stewart et al., 1993), and may be useful as an indirect measure of myelination within the brain. An example *MWF* map is shown in Figure 13. Note that the relative fraction of the signal within the myelin water component is relatively small (<20%) and the *T2* of this component is relatively short (<30 msec) such that short echo spacings (<10 msec) are necessary to be able to sense it.

MWF may be measured using a more traditional multiecho CPMG experiment described above with typically 32 echoes or more. There are several challenges associated with this kind of measurement in addition to issues related to stimulated echoes and RF inhomogeneities present in single component *T2* measurements. The short *T2* of the myelin water favors CPMG sequences with very short echo spacing to obtain an accurate and precise estimate of the short *T2* signal (Dula et al., 2009). The estimation of the multiple *T2* components and times is typically performed using a nonnegative least squares algorithm with a multi-component exponential decay function and is highly sensitive to measurement noise and errors (Whittall and Mackay, 1989). Some form of data regularization is also needed, as the model is usually highly underdetermined. This analysis also assumes no exchange of water between the compartments over the time scale of the measurement (typically 128–320 msec for 32 echoes and 4–10 msec echo spacing). Recent studies suggest that exchange rates may differ substantially with differing myelin thickness, causing a systematic underestimation of *MWF* for faster exchange rates (i.e., thinner myelin) (Dula et al., 2010). Standard two-dimensional (2D) multiple spin echo sequences often have imperfect RF pulses, which will lead to stimulated echo pathways in the echo train and potentially bias the *T2* measurements. To minimize the image noise and bias errors in the echo signals, these measurements are typically performed using a single-slice 2D CPMG sequence with thick slices (4 mm or more), hard or composite RF pulses, and variable-amplitude gradient-crusher schemes with a total scan time of 12–20 min. Thus, the spatial coverage is limited and the method is fairly inefficient for characterizing the *MWF* or *T2* for multiple slices. A 3D CPMG version of this method has been demonstrated, which improves the coverage and improve the overall sensitivity through increased signal averaging (Mädler and MacKay, 2006).

Multicomponent behavior has also been observed in 3D steady-state SPGR (Deoni et al., 2007) and SSFP (Deoni et al., 2008b) sequences. This has recently led to the development of a multi-component version of DESPOT (mcDESPOT) (Deoni et al., 2008a) that is able to generate whole-brain *MWF* maps at 1.5–2.0 mm resolution with scan times similar to traditional single-slice CPMG MET2 methods (10–20 min). The current mcDESPOT signal model includes two (fast and slow) *T1* and *T2* components, an exchange time constant, and the relative signal fractions of the components. The signal with the short *T1* and *T2* is assumed to originate from the myelin water in WM. An issue is that this model is mathematically complex. It has issues with nonconvergence due to local minima and requires computationally intensive nonlinear stochastic global optimization methods (Berger and Silverman, 1991) to converge to a reasonable solution. The model will also not properly converge for in tissues with long T2 species like either CSF or edema although convergence may be improved by adding a nonexchanging long *T2* compartment at the cost of even further computational complexity (Deoni, 2011). Despite some of these issues, multicomponent relaxometry with steady-state sequences is

promising for characterizing myelin water over the entire brain in a time feasible for many research applications.

Applications of relaxometry stains to characterize WM

Single-component relaxometry stains are sensitive, although nonspecific, to subtle differences in the microstructure of WM tracts. Studies in healthy individuals have shown that *T1* times in specific WM tracts differ over a range of 640–836 msec at 1.5T (Yarnykh, 2004, 2009; Yarnykh and Yuan, 2004), while tract *T2** values between 48.8 and 57.0 msec have been observed at 3T (Cherubini et al., 2009). A more direct application to measuring brain connectivity is through the introduction of manganese as a tracer. Manganese is taken up by the calcium channels of the axons and follows transynaptic connections across distant brain regions. It is also a paramagnetic *T1* shortening agent. While many studies utilize *T1w* imaging, *T1* mapping can be used to make accurate measurements of *in vivo* tracer concentration (Kim et al., 2011).

MWF is of particular interest as this stain is most closely associated with myelination and myelin geometry, which have a significant impact on the conduction velocity of WM connections (Smith and Koles, 1970). *MWF* as measured with MET2 is highly correlated with myelin content in profoundly demyelinating diseases such as MS (Tozer et al., 2005), although much less so among subtle variations in healthy myelinated tracts (Dula et al., 2010). Whole-brain mcDESPOT studies in a canine *sh* pup model of dysmyelination have also shown substantially diminished *MWF* consistent with the paucity of myelin in the affected animals (Hurley et al., 2010). Recent human mcDESPOT studies have showed an increase in the WM *MWF* with brain development in children from birth up to 5 years of age (Deoni et al., 2011). The mcDESPOT *MWF* also appears to be affected in both lesions and NAWM in patients with MS and these changes appeared to relate to the degree of clinical severity (Kitzler et al., 2011). *MWF* is a promising stain for characterizing the myelination of WM tracts, although further work needs to be done to investigate its sensitivity to small variations in myelination and how it is affected by different microstructural properties such as myelin thickness, g-ratio, overall myelin content, differentiation between intact versus damaged myelin, and exchange of water between myelin and nonmyelin compartments. These are critical issues for using *MWF* to assess and track myelin repair therapies.

Other Methods for Characterizing WM

Although the vast majority of recent MRI studies of WM have focused on diffusion, MT, or relaxometry, there are other techniques that may provide complementary information. One of the oldest methods is MR spectroscopy (MRS), which may be used to characterize specific metabolites in the tissue, including N-acetylaspartate (NAA), creatine, choline, and neurotransmitters like gamma-aminobutyric acid (GABA) and glutamine/glutamate. Each of these metabolites reflects different physiological processes and has unique spectral signatures. Of significant interest in WM is NAA, which is a marker of the presence, density, and health of neurons, including the axonal processes. In fact, NAA may be one of the most specific markers of healthy axons and, as such, it is surprising that it is not used more widely for the investigation of WM in the brain. This may be due in part to the fact that MRS is extremely sensitive to the homogeneity of the magnetic field, which makes it challenging to apply in areas near air or bone interfaces. The concentrations of the metabolites are also in the micromolar range (compare with multiple molar for water); thus, large voxels must be used and the acquisition speed is slow. Therefore, MRS studies are often limited by poor coverage, poor resolution, and long scan times.

The recent push toward ever higher magnetic fields makes qMRI methods more challenging. Imaging distortions in DTI studies increase proportional to the field strength. The RF power deposition (specific absorption rate) increases quadratically with the magnetic field strength, which limits the application of MT pulses and can also limit the flip angles used in steady-state imaging. However, susceptibility weighted imaging is one method that greatly benefits from higher magnetic field strengths. Recent studies have observed interesting contrast in WM tracts as a function of orientation and degree of myelination (Liu et al., 2012). Stunning images of WM tracts have recently been obtained in *ex vivo* brain specimens (Sati et al., 2012). Techniques for characterizing WM in the human brain are only beginning to be developed.

Other WM cellular components are the glia, which include oligodendrocytes, astrocytes, and microglia. In general, there are no specific markers of changes in either oligodendrocytes or astrocytes. Recent evidence suggests that hypointense WM lesions on T1w imaging may indicate reactive astrocytes (Sibson et al., 2008). Increases in microglia often accompany inflammation, which can be detected using contrast agents, either gadolinium or superparamagnetic iron oxide (SPIO) particles. Recent studies have suggested that SPIO particles are preferentially taken up by macrophages in inflammatory regions. The impact of these contrast agents on other qMRI measures has not (Oweida et al., 2004) been widely studied, and thus multimodal imaging studies must be designed carefully.

Multimodal Imaging

Many of the qMRI measures appear to demonstrate sensitivity to myelinated WM; in general, *MWF*, *BPF*, and *FA* all are increased and *DR* is decreased in myelinated WM relative to GM, whereas demyelinating WM lesions all show reversed trends in these measures. Note that in areas of crossing WM tracts, the relationship of *FA* and *DR* with myelination is likely to be less predictable. However, the qMRI methods are sensitive to different mechanisms and therefore are potentially complementary. For example, either the *BPF* from qMT or the *MWF* from relaxometry might be able to provide more specific information than either *FA* or *DR* from DTI regarding myelin changes in brain areas with crossing WM tracts. While both the MT and *T2* relaxometry appear to be more specific to myelin, head-to-head comparisons have showed poor correspondence. A comparison of the *MTR* and the *MWF* in both healthy controls and MS patients did not show any correlations in GM or NAWM, but did demonstrate a modest correlation in MS lesions ($r = 0.5$) (Vavasour et al., 1998). This may be due to the differences in the mechanisms—the *MWF* will be sensitive to the spacing of the myelin membranes, whereas MT effects are more sensitive to the presence of proteins and other macromolecules in the myelin bilayers. Recently, a few studies have applied multiple contrast mechanisms to

Table 1. Comparison of Different Quantitative Magnetic Resonance Imaging Analysis Approaches

Method	*Manual effort*	*Spatial normalization*	*Native space*	*Localization*	*Statistical power*
Histogram			×	−−−	+++
Manual ROI	×		×	+	++
Atlas template		×	×[a]	+	++
Tractography	×[b]		×	+	++
VBA		×		++	−−−
T-SPOON VBA		×		++	−−
TBSS		×	×	++	−

Analyses method properties are described in each row. Properties are listed in columns. × denotes that the method has the specific property. In the Localization and Statistical power columns, the number of + and − symbols indicates the relative strength or weakness, respectively, in those categories.

[a]Atlas templates may be applied in either native or normalized spaces.

[b]Automated tract constraints may be applied to define tracts.

ROI, region-of-interest; VBA, voxel-based analysis; T-SPOON, tissue specific, smoothing compensated VBA; TBSS, tract-based spatial statistics.

investigate WM differences. Several studies attempted to investigate the association between qMT measures and DTI parameters (Stikov et al., 2011; Underhill et al., 2009). They observed the weak correlation between *BPF* and *FA* in the WM of human brain; however, strong correlations between DTI and qMT parameters were found in GM (Underhill et al., 2009). It was concluded that the lack of correlations between qMT and DTI parameters in WM comes from the differences in the physical principle of these two methods as DTI parameters are dependent on the direction of fibers while qMT parameters are also associated myelination level and with the density of myelinated fibers (Underhill et al., 2009). A comparison of qMT (*BPF*) and DTI measures in fixed brain tissue from a dysmyelinated, shiverer mouse model showed decreased *BPF* and increased *DR* in dysmyelinated WM with a modest correlation ($r = 0.57$) between *BPF* and *DR* in WM (Ou et al., 2009). Gender comparisons in regional corpus callosum measurements of both DTI measures and *T2 MWF* showed weak correlations between *MWF* and both *FA* and *DR* ($r = 0.39$ and 0.35, respectively) and the regional significance by gender was not consistent for DTI and *MWF* (Liu et al., 2010). A couple of studies have compared *MWF* and BPF measurements in WM. Tozer and associates (2005) found a negligible correlation between these measures in NAWM of MS patients. Another more recent study reported that the qMTI measures, including *BPF*, were much more sensitive than MET2 relaxometry to temporal changes associated with the disease in MS lesions, though it has been reported that qMT is also sensitive to inflammatory processes (Levesque et al., 2010). An aging study of several qMRI measures (DTI *FA* and *MD*, *MTR*, and *T1*, *T2*, *T2** relaxation times) in healthy adults versus age (range 18–85 years) revealed distinct age-related trajectories and spatial patterns for each of the qMRI measures (Draganski et al., 2011).

A number of studies have also combined MRS and qMRI measures. As discussed above, the NAA from MRS is often described as a fairly specific marker of viable neurons and axons in WM. A summary of a few of these studies is included here. A small ($N = 8$) study comparing NAA and *MTR* in frontal WM of patients with late-onset depression showed a high correlation ($r = 0.89$) (McLean and Barker, 2006). An older study comparing NAA and *MTR* in ($N = 13$) patients found strong correlations ($r = 0.73$) in WM lesions (Kimura et al., 1996). A DTI study ($N = 25$) of small vessel disease reported modest correlations between NAA and either *FA* or *MD* ($r \sim 0.5$) in the centrum semiovale, a region with significant fiber crossings (Nitkunan et al., 2006). A recent study of 15 MS patients showed no relationship in the splenium of the corpus callosum between NAA and *FA* (Cader et al., 2007). In that study, they concluded that the changes in *FA* were from axon loss, which was not detected by differences in NAA. Conversely, an MRS versus DTI *FA* study of glioma patients found a high correlation between NAA and *FA* in and around the tumor ($r > 0.94$), but the relationship was much more modest in NAWM ($r \sim 0.5$) (Goebell et al., 2006). A comparison of high *b*-value *q*-space imaging (DSI) and MRS showed modest correlations between the NAA and both the *MSD* and the zero-displacement probability ($r = 0.61$ and 0.54, respectively) (Assaf et al., 2005). The relationship between NAA and MWF has largely been unexplored.

The inconsistent correlations between these WM measures suggest either that the measures are reflecting different physiological features of the WM or that the measures are fairly noisy. In reality, it is probably a combination of both factors. It should be noted that there is considerable variability in the measurement protocols and analysis methods for each of the qMRI modalities, which greatly influences the accuracy and variance of the measurements.

Analyses of qMRI Stain Maps

The analyses of qMRI maps are particularly challenging because many of the measures are extremely heterogeneous across the brain. For example, the *FA* values in healthy WM can range from roughly 0.2 up to nearly 1.0. However, within a fixed and small region of WM (e.g., the genu of the corpus callosum or the posterior limb of the internal capsule), it is possible to compare values between individuals, though it is critical to use methods with anatomic specificity. There are many strategies for comparing qMRI measurements between subjects with their relative strengths and weaknesses. Table 1 lists different analysis strategies and the relative merits and weaknesses. The simplest approach is to compute a whole brain histogram at the obvious sacrifice of anatomical specificity. The three primary strategies for obtaining region-specific measures are (1) manual segmentation of a ROI,

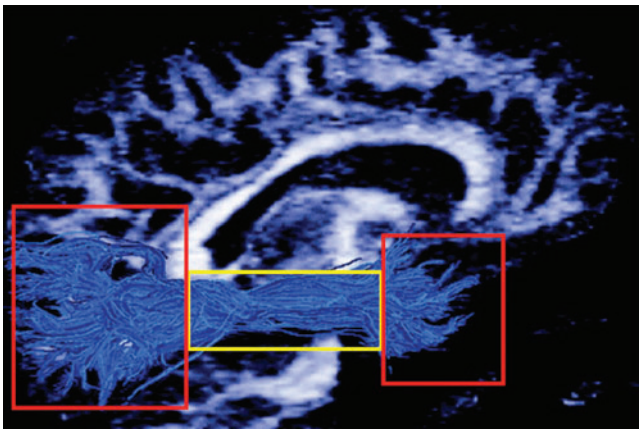

FIG. 15. Illustration of strengths and weakness of using tractography for regional brain segmentation. In this case, the trunk of the inferior longitudinal fasciuculus is a tight coherent bundle; however, the regions near the ends of the tract show considerable branching and divergence, which is likely to vary considerably across subjects.

which can be extremely tedious, (2) automated application of an atlas-based template to the DTI data, and (3) tractography-based segmentation of specific WM pathways. Tract-based analyses based upon tractography have appeal for obvious reasons, though the confidence of the qMRI measures is higher in the trunk of the reconstructed tract and less so at branches and the periphery (see Fig. 15). More generic analyses of regional differences may be tested using voxel-based analysis (VBA) methods similar to voxel-based morphometry (Ashburner and Friston, 2000). An advantage of VBA methods is that differences may be detected anywhere without any specific *a priori* anatomic hypotheses, though the statistical power is much reduced. An issue with VBA is that the image processing steps—spatial normalization and blurring—introduce more partial volume averaging, which causes mixing of different tissue types (e.g., WM and GM or CSF) and makes the analysis sensitive to morphology differences, such as might be present between experimental groups being compared. Recent VBA strategies—T-SPOON (tissue-specific, smoothing-compensated VBA) (Lee et al., 2009) and tract-based spatial statistics (TBSS) (Smith et al., 2006)—help to ameliorate some of these limitations. An important step for several of these analysis methods is spatial normalization, which attempts to co-register the anatomic-specific qMRI measures across subjects. Recent advances in nonlinear, diffeomorphic spatial normalization methods (Zhang et al., 2010) and full diffusion tensor matching and reorientation (Zhang et al., 2006) (see Fig. 16) significantly improve the anatomic correspondence between subjects.

Summary and Future of the Field

In summary, we have presented several qMRI measures or stains that are promising for characterizing WM *in vivo*. Diffusion MRI (including DTI), MT, and relaxometry are all sensitive measures of myelination and axons; however, each is based upon different mechanisms. Further, the specificity of these measures to specific WM properties like the degree of myelination is less clear and many questions remain.

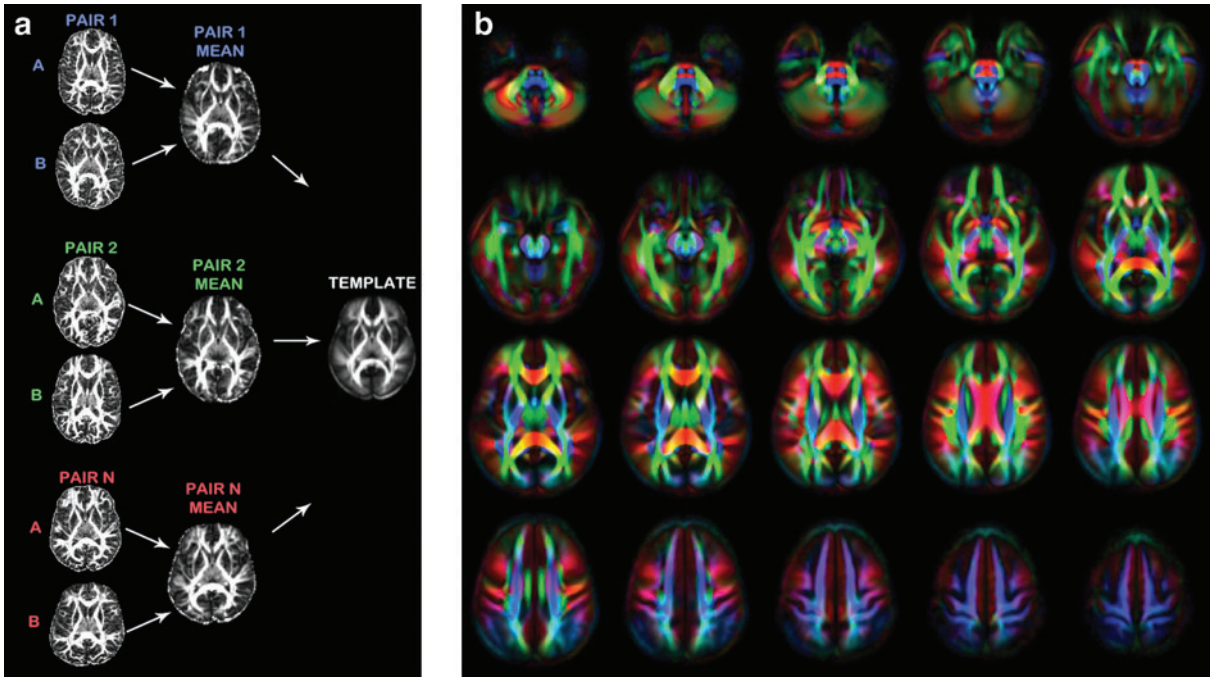

FIG. 16. Spatial normalization example for DTI data. In this example a two-step normalization is illustrated. **(a)** Pairs of images (e.g., longitudinal or twin) are normalized with each other, followed by normalization to an overall population averaged template. The spatial normalization employed a diffeomorphic warping algorithm with tensor reorientation. **(b)** The normalization shows good correspondence of most major WM features, though there is still considerable variation in smaller and more peripheral tracts.

Diffusion MRI is modulated by the presence and spacing of membranes and any other barriers, which include the myelin membranes as well as any other cellular structures in the WM. MT is sensitive not only to the myelin proteins, but also to any other proteins and any other macromolecules, such as those found in regions of inflammation. The short *T2* signal from the water trapped in the myelin bilayers appears to be fairly specific, though the actual quantification in terms of the amount of myelination is more challenging.

An important perspective to maintain in the interpretation of these qMRI stains is that all of these measures are modulations of the water signal. A change in the overall amount of water in a region of tissue will significantly influence the qMRI measure irrespective of the axonal properties. For example, edema will increase the extracellular water fraction, which will impact all of the qMRI measures described here. A decreased *MWF* or increased *DR* in a region of WM with edema does not necessarily reflect a decreased level of myelination. The size of the voxels is also very large relative to the cellular structural features that are being characterized. A 1-mm cubic voxel may contain more than a thousand axons (1–20 μm in diameter), which may have a broad range of diameters, degree of myelination, and numbers and types of glia; thus, these images are very course and blurred maps of the microstructural detail.

The qMRI stain maps are all derived from multiple contrast-weighted images, which causes these imaging methods to be sensitive to misregistration from head motion, measurement noise, and artifacts in any of the images. Thus, it is critical to carefully review individual image quality and the registration fidelity before computing quantitative maps. The calculation of the quantitative measures often uses highly nonlinear models with multiple local energy minima in the solution space, making them highly sensitive to the measurement noise. These measurement noise effects can subsequently lead to biased estimates with high variance. If the noise is too high to achieve reliable estimates, then either scan time should be increased or spatial resolution decreased. Ideally, the SNR of the original image measurements should be reported in publications to be able to assess the level of image quality. Studies are also needed to determine SNR cutoff thresholds below which the calculations are either biased or unstable. While obtaining multiple qMRI measures in a single study is appealing, the scan time can be considerable—for example, DTI is on the order of 10 min and qMT and multicomponent relaxometry are on the order of 20–30 min or more each. Thus, if imaging time is limited, it is probably preferable to spend more time on a single qMRI measure or chose simpler measures that can be estimated from smaller data sets (e.g., *MD* instead of the full diffusion tensor, or *T1* with B1 calibration instead of *MWF*). Current and future improvements to coil sensitivity design, parallel imaging, and constrained reconstruction methods for undersampled multiparametric image data (Velikina et al., 2011) may be used to significantly accelerate acquisition times and/or improve the measurement accuracy.

Note that there is an inherent trade-off between resolution and SNR. In general, imaging can accurately resolve signal from structures that are at least twice as large as the resolution. If the imaging resolution dimension is larger, then the minimum resolvable structure size likewise increases. For smaller structures (e.g., fornix and cingulum bundles), the measurements will have some partial volume averaging, which makes it difficult to disambiguate the microstructural properties from the macrostructure. Another consideration is that as long as the SNR is not too low (>3–4) for any of the images, the SNR can be improved by spatial smoothing so obtaining DW images at the highest possible resolution is a reasonable strategy. The concept of superresolution tractography is particularly exciting and novel and may provide details beyond the inherent image resolution; however, the quantitative measures along those pathways may still have partial volume averaging effects.

To apply these qMRI stains to multicenter clinical trials, it is necessary to develop standardized acquisition protocols that include methods to correct for errors and inhomogeneities in both B0 (static field strength/frequency) and B1 (flip angle). This is currently challenged by differences in pulse sequences on different scanner platforms. Phantom materials with specific qMRI properties may be useful for comparing measurements across scanners and sites. Further, while there are a growing number of software tools for calculating and analyzing DTI images, there are no widely available tools for either qMT or multicomponent relaxometry, which limits their application to more technically advanced research groups.

DTI has clearly been the most widely used method for investigating and describing structural connectivity properties in the brain. As the field moves forward, it is critical to also investigate MT and relaxometry measures along specific WM pathways to obtain complementary and potentially more specific information about the biological properties of these connections. Relevant to this point, there is still a lot that is not known about the mechanisms of these qMRI measures and how they are influenced by subtle variations in CNS pathology. More detailed and specific studies that relate WM histology and pathology to qMRI measures are essential to move this field forward and make the interpretation of these measurements more clear.

The recent work in mapping the global networks or connectomes of structural connectivity using tractography-based approaches is extremely exciting and has generated considerable enthusiasm in the neuroscience community. However, we must remember that these networks represent abstractions of the real structural brain connections through the modulation of water diffusion properties by the WM microstructure. Sophisticated mathematical models are being applied to characterize these networks, which hopefully reflect the structural properties of biological substrates that we are trying to characterize. How to define and/or interpret connectivity based upon structural connectomes is a work in progress. To date, connectome studies have focused on DTI/DWI properties based upon tractography properties; however, future connectome studies may also incorporate other WM measures like the *FA*, the *BPF*, or the *MWF*.

After these methods are standardized, qMRI stain atlases can be generated as a function of age, gender, disease, and or trait measure. Either tractography-based or morphologic-based templates of WM regions or structures can be used to characterize WM properties across populations. Integration of these atlases and tract-based measures may subsequently be compared against functional connectivity measures. This integration of qMRI stains with functional connectivity will provide a more complete picture of brain connectivity properties.

Acknowledgments

The authors acknowledge support from several relevant grants that supported and inspired some of this work, including NICHD P30 HD003352 (A.L.A.), NIMH P50 MH84051 (A.L.A.), NIMH RO1 MH080826 (A.L.A.), NINDS RO1 NS065034 (A.A.S.), NINDS RO1 NS050466 (A.S.F.), the National MS Society (A.L.A., A.A.S., and A.S.F.), and the Morgridge Institutes for Research (MIR-University of Wisconsin, NA). The authors are also grateful for figure contributions from Fernando Calamante and Vasily Yarnykh. Figure 12 has been reprinted from Yarnykh and Yuan, Copyright (2004), with permission from Elsevier.

Author Disclosure Statement

No competing financial interests exist.

References

Adluru N, Zhang H, Fox AS, Shelton SE, Ennis CM, Bartosic AM, Oler JA, Tromp do PM, Zakszewski E, Gee JC, Kalin NH, Alexander AL. 2012. A diffusion tensor brain template for Rhesus Macaques. Neuroimage 59:306–318.

Alexander AL, Hasan K, Kindlmann G, Parker DL, Tsuruda JS. 2000. A geometric analysis of diffusion tensor measurements of the human brain. Magn Reson Med 44:283–291.

Alexander AL, Hasan KM, Lazar M, Tsuruda JS, Parker DL. 2001. Analysis of partial volume effects in diffusion-tensor MRI. Magn Reson Med 45:770–780.

Alexander AL, Lee JE, Lazar M, Field AS. 2007. Diffusion tensor imaging of the brain. Neurotherapeutics 4:316–329.

Alexander DC, Barker GJ, Arridge SR. 2002. Detection and modeling of non-Gaussian apparent diffusion coefficient profiles in human brain data. Magn Reson Med 48:331–340.

Alfano B, Brunetti A, Covelli EM, Quarantelli M, Panico MR, Ciarmiello A, Salvatore M. 1997. Unsupervised, automated segmentation of the normal brain using a multispectral relaxometric magnetic resonance approach. Magn Reson Med 37:84–93.

Anderson AW. 2001. Theoretical analysis of the effects of noise on diffusion tensor imaging. Magn Reson Med 46:1174–1188.

Armstrong CL, Traipe E, Hunter JV, Haselgrove JC, Ledakis GE, Tallent EM, Shera D, van Buchem MA. 2004. Age-related, regional, hemispheric, and medial-lateral differences in myelin integrity in vivo in the normal adult brain. AJNR Am J Neuroradiol 25:977–984.

Ashburner J, Friston KJ. 2000. Voxel-based morphometry—the methods. Neuroimage 11:805–821.

Ashtari M, Cervellione KL, Hasan KM, Wu J, McIlree C, Kester H, Ardekani BA, Roofeh D, Szeszko PR, Kumra S. 2007. White matter development during late adolescence in healthy males: a cross-sectional diffusion tensor imaging study. Neuroimage 35:501–510.

Assaf Y, Basser PJ. 2005. Composite hindered and restricted model of diffusion (CHARMED) MR imaging of the human brain. Neuroimage 27:48–58.

Assaf Y, Ben-Bashat D, Chapman J, Peled S, Biton IE, Kafri M, Segev Y, Hendler T, Korczyn AD, Graif M, Cohen Y. 2002. High b-value q-space analyzed diffusion-weighted MRI: application to multiple sclerosis. Magn Reson Med 47:115–126.

Assaf Y, Chapman J, Ben-Bashat D, Hendler T, Segev Y, Korczyn AD, Graif M, Cohen Y. 2005. White matter changes in multiple sclerosis: correlation of q-space diffusion MRI and 1H MRS. Magn Reson Imaging 23:703–710.

Assaf Y, Cohen Y. 2000. Assignment of the water slow-diffusing component in the central nervous system using q-space diffusion MRS: implications for fiber tract imaging. Magn Reson Med 43:191–199.

Assemlal HE, Tschumperle D, Brun L. 2009. Efficient and robust computation of PDF features from diffusion MR signal. Med Image Anal 13:715–729.

Au Duong MV, Boulanouar K, Audoin B, Treseras S, Ibarrola D, Malikova I, Confort-Gouny S, Celsis P, Pelletier J, Cozzone PJ, Ranjeva JP. 2005. Modulation of effective connectivity inside the working memory network in patients at the earliest stage of multiple sclerosis. Neuroimage 24:533–538.

Bagary MS, Symms MR, Barker GJ, Mutsatsa SH, Joyce EM, Ron MA. 2003. Gray and white matter brain abnormalities in first-episode schizophrenia inferred from magnetization transfer imaging. Arch Gen Psychiat 60:779–788.

Bar-Shir A, Avram L, Ozarslan E, Basser PJ, Cohen Y. 2008. The effect of the diffusion time and pulse gradient duration ratio on the diffraction pattern and the structural information estimated from q-space diffusion MR: experiments and simulations. J Magn Reson 194:230–236.

Bar-Shir A, Duncan ID, Cohen Y. 2009. QSI and DTI of excised brains of the myelin-deficient rat. Neuroimage 48:109–116.

Barrick TR, Clark CA. 2004. Singularities in diffusion tensor fields and their relevance in white matter fiber tractography. Neuroimage 22:481–491.

Basser PJ. 1997. New histological and physiological stains derived from diffusion-tensor MR images. Ann N Y Acad Sci 820:123–138.

Basser PJ, Mattiello J, LeBihan D. 1994. MR diffusion tensor spectroscopy and imaging. Biophys J 66:259–267.

Basser PJ, Pajevic S, Pierpaoli C, Duda J, Aldroubi A. 2000. In vivo fiber tractography using DT-MRI data. Magn Reson Med 44:625–632.

Basser PJ, Pierpaoli C. 1996. Microstructural and physiological features of tissues elucidated by quantitative-diffusion-tensor MRI. J Magn Reson Series B 111:209–219.

Bassett DS, Brown JA, Deshpande V, Carlson JM, Grafton ST. 2011. Conserved and variable architecture of human white matter connectivity. Neuroimage 54:1262–1279.

Bava S, Thayer R, Jacobus J, Ward M, Jernigan TL, Tapert SF. 2010. Longitudinal characterization of white matter maturation during adolescence. Brain Res 1327:38–46.

Beaulieu C, Allen PS. 1994. Water diffusion in the giant axon of the squid: implications for diffusion-weighted MRI of the nervous system. Magn Reson Med 32:579–583.

Ben Bashat D, Ben Sira L, Graif M, Pianka P, Hendler T, Cohen Y, Assaf Y. 2005. Normal white matter development from infancy to adulthood: comparing diffusion tensor and high b value diffusion weighted MR images. J Magn Reson Imaging 21:503–511.

Berger MF, Silverman HF. 1991. Microphone array optimization by stochastic region contraction. IEEE Trans Sig Proc 39:2377–2386.

Berry I, Barker GJ, Barkhof F, Campi A, Dousset V, Franconi JM, Gass A, Schreiber W, Miller DH, Tofts PS. 1999. A multicenter measurement of magnetization transfer ratio in normal white matter. J Magn Reson Imaging 9:441–446.

Biton IE, Duncan ID, Cohen Y. 2007. q-Space diffusion of myelin-deficient spinal cords. Magn Reson Med 58:993–1000.

Cader S, Johansen-Berg H, Wylezinska M, Palace J, Behrens TE, Smith S, Matthews PM. 2007. Discordant white matter N-acetylasparate and diffusion MRI measures suggest that chronic metabolic dysfunction contributes to axonal pathology in multiple sclerosis. Neuroimage 36:19–27.

Calamante F, Tournier JD, Jackson GD, Connelly A. 2010. Track-density imaging (TDI): super-resolution white matter imaging using whole-brain track-density mapping. Neuroimage 53:1233–1243.

Calamante F, Tournier JD, Smith RE, Connelly A. 2012. A generalised framework for super-resolution track-weighted imaging. Neuroimage 59:2494–2503.

Callaghan PT. 1996. NMR imaging, NMR diffraction and applications of pulsed gradient spin echoes in porous media. Magn Reson Imaging 14:701–709.

Caspers S, Eickhoff SB, Rick T, von Kapri A, Kuhlen T, Huang R, Shah NJ, Zilles K. 2011. Probabilistic fibre tract analysis of cytoarchitectonically defined human inferior parietal lobule areas reveals similarities to macaques. Neuroimage 58:362–380.

Cercignani M, Alexander DC. 2006. Optimal acquisition schemes for in vivo quantitative magnetization transfer MRI. Magn Reson Med 56:803–810.

Chang LC, Jones DK, Pierpaoli C. 2005. RESTORE: robust estimation of tensors by outlier rejection. Magn Reson Med 53:1088–1095.

Chen JT, Collins DL, Freedman MS, Atkins HL, Arnold DL. 2005. Local magnetization transfer ratio signal inhomogeneity is related to subsequent change in MTR in lesions and normal-appearing white-matter of multiple sclerosis patients. Neuroimage 25:1272–1278.

Chen JT, Kuhlmann T, Jansen GH, Collins DL, Atkins HL, Freedman MS, O'Connor PW, Arnold DL. 2007. Voxel-based analysis of the evolution of magnetization transfer ratio to quantify remyelination and demyelination with histopathological validation in a multiple sclerosis lesion. Neuroimage 36:1152–1158.

Chenevert TL, Brunberg JA, Pipe JG. 1990. Anisotropic diffusion in human white matter: demonstration with MR techniques in vivo. Radiology 177:401–405.

Cheng HL, Wright GA. 2006. Rapid high-resolution T(1) mapping by variable flip angles: accurate and precise measurements in the presence of radiofrequency field inhomogeneity. Magn Reson Med 55:566–574.

Cheng P, Magnotta VA, Wu D, Nopoulos P, Moser DJ, Paulsen J, Jorge R, Andreasen NC. 2006. Evaluation of the GTRACT diffusion tensor tractography algorithm: a validation and reliability study. Neuroimage 31:1075–1085.

Cherubini A, Péran P, Hagberg GE, Varsi AE, Luccichenti G, Caltagirone C, Sabatini U, Spalletta G. 2009. Characterization of white matter fiber bundles with T2*relaxometry and diffusion tensor imaging. Magn Reson Med 61:1066–1072.

Cheung MM, Hui ES, Chan KC, Helpern JA, Qi L, Wu EX. 2009. Does diffusion kurtosis imaging lead to better neural tissue characterization? A rodent brain maturation study. Neuroimage 45:386–392.

Chiu CH, Lo YC, Tang HS, Liu IC, Chiang WY, Yeh FC, Jaw FS, Tseng WY. 2011. White matter abnormalities of fronto-striato-thalamic circuitry in obsessive-compulsive disorder: a study using diffusion spectrum imaging tractography. Psychiatry Res 192:176–182.

Christensen KA, Grant DM, Schulman EM, Walling C. 1974. Optimal determination of relaxation times of fourier transform nuclear magnetic resonance. Determination of spin-lattice relaxation times in chemically polarized species. J Phys Chem 78:1971–1977.

Chung HW, Chou MC, Chen CY. 2011a. Principles and limitations of computational algorithms in clinical diffusion tensor MR tractography. AJNR Am J Neuroradiol 32:3–13.

Chung MK, Adluru N, Dalton KM, Alexander AL, Davidson RJ. 2011b. Scalable brain network construction on white matter fibers. In: Dawant BM, Haynor DR (eds.) *SPIE Medical Imaging 2011: Image Processing*. Lake Buena Vista, FL: Society of Photo-Optical Instrumentation Engineers (SPIE); p. 79624G.

Clark CA, Le Bihan D. 2000. Water diffusion compartmentation and anisotropy at high b values in the human brain. Magn Reson Med 44:852–859.

Close TG, Tournier JD, Calamante F, Johnston LA, Mareels I, Connelly A. 2009. A software tool to generate simulated white matter structures for the assessment of fibre-tracking algorithms. Neuroimage 47:1288–1300.

Conturo TE, Lori NF, Cull TS, Akbudak E, Snyder AZ, Shimony JS, McKinstry RC, Burton H, Raichle ME. 1999. Tracking neuronal fiber pathways in the living human brain. Proc Natl Acad Sci U S A 96:10422–10427.

Cory DG, Garroway AN. 1990. Measurement of translational displacement probabilities by NMR: an indicator of compartmentation. Magn Reson Med 14:435–444.

Dauguet J, Peled S, Berezovskii V, Delzescaux T, Warfield SK, Born R, Westin CF. 2007. Comparison of fiber tracts derived from in-vivo DTI tractography with 3D histological neural tract tracer reconstruction on a macaque brain. Neuroimage 37:530–538.

Davies GR, Tozer DJ, Cercignani M, Ramani A, Dalton CM, Thompson AJ, Barker GJ, Tofts PS, Miller DH. 2004. Estimation of the macromolecular proton fraction and bound pool T2 in multiple sclerosis. Mult Scler 10:607–613.

de Zeeuw P, Mandl RC, Hulshoff Pol HE, van Engeland H, Durston S. 2011. Decreased frontostriatal microstructural organization in attention deficit/hyperactivity disorder. Hum Brain Mapp [Epub ahead of print]; DOI: 10.1002/hbm.21335

Deloire-Grassin MS, Brochet B, Quesson B, Delalande C, Dousset V, Canioni P, Petry KG. 2000. In vivo evaluation of remyelination in rat brain by magnetization transfer imaging. J Neurol Sci 178:10–16.

Deoni SC. 2007. High-resolution T1 mapping of the brain at 3T with driven equilibrium single pulse observation of T1 with high-speed incorporation of RF field inhomogeneities (DESPOT1-HIFI). J Magn Reson Imaging 26:1106–1111.

Deoni SC, Josseau MJ, Rutt BK, Peters TM. 2005a. Visualization of thalamic nuclei on high resolution, multi-averaged T1 and T2 maps acquired at 1.5 T. Hum Brain Mapp 25:353–359.

Deoni SC, Peters TM, Rutt BK. 2005b. High-resolution T1 and T2 mapping of the brain in a clinically acceptable time with DESPOT1 and DESPOT2. Magn Reson Med 53:237–241.

Deoni SC, Rutt BK, Arun T, Pierpaoli C, Jones DK. 2008a. Gleaning multicomponent T1 and T2 information from steady-state imaging data. Magn Reson Med 60:1372–1387.

Deoni SC, Rutt BK, Jones DK. 2007. Investigating the effect of exchange and multicomponent T(1) relaxation on the short repetition time spoiled steady-state signal and the DESPOT1 T(1) quantification method. J Magn Reson Imaging 25:570–578.

Deoni SC, Rutt BK, Jones DK. 2008b. Investigating exchange and multicomponent relaxation in fully-balanced steady-state free precession imaging. J Magn Reson Imaging 27: 1421–1429.

Deoni SC, Rutt BK, Peters TM. 2003. Rapid combined T1 and T2 mapping using gradient recalled acquisition in the steady state. Magn Reson Med 49:515–526.

Deoni SCL. 2009. Transverse relaxation time (T2) mapping in the brain with off-resonance correction using phase-cycled steady-state free precession imaging. J Magn Reson Imaging 30:411–417.

Deoni SCL. From 3 to 3: Introducing a Third 'Free' Water Component into mcDESPOT. International Workshop on Advanced White Matter Imaging, Reykjavik, Iceland, 2011, p. 12.

Deoni SCL, Mercure E, Blasi A, Gasston D, Thomson A, Johnson M, Williams SCR, Murphy DGM. 2011. Mapping infant brain myelination with magnetic resonance imaging. J Neurosci 31:784–791.

Descoteaux M, Deriche R, Le Bihan D, Mangin JF, Poupon C. 2011. Multiple q-shell diffusion propagator imaging. Med Image Anal 15:603–621.

Dousset V, Brochet B, Vital A, Gross C, Benazzouz A, Boullerne A, Bidabe AM, Gin AM, Caille JM. 1995. Lysolecithin-induced demyelination in primates: preliminary in vivo study with MR and magnetization transfer. AJNR Am J Neuroradiol 16:225–231.

Dousset V, Grossman RI, Ramer KN, Schnall MD, Young LH, Gonzalez-Scarano F, Lavi E, Cohen JA. 1992. Experimental allergic encephalomyelitis and multiple sclerosis: lesion characterization with magnetization transfer imaging. Radiology 182:483–491.

Draganski B, Ashburner J, Hutton C, Kherif F, Frackowiak RS, Helms G, Weiskopf N. 2011. Regional specificity of MRI contrast parameter changes in normal ageing revealed by voxel-based quantification (VBQ). Neuroimage 55:1423–1434.

Dula AN, Gochberg DF, Does MD. 2009. Optimal echo spacing for multi-echo imaging measurements of Bi-exponential T2 relaxation. J Magn Reson 196:149–156.

Dula AN, Gochberg DF, Valentine HL, Valentine WM, Does MD. 2010. Multiexponential T2, magnetization transfer, and quantitative histology in white matter tracts of rat spinal cord. Magn Reson Med 63:902–909.

Dyrby TB, Sogaard LV, Parker GJ, Alexander DC, Lind NM, Baare WF, Hay-Schmidt A, Eriksen N, Pakkenberg B, Paulson OB, Jelsing J. 2007. Validation of in vitro probabilistic tractography. Neuroimage 37:1267–1277.

Ennis DB, Kindlmann G. 2006. Orthogonal tensor invariants and the analysis of diffusion tensor magnetic resonance images. Magn Reson Med 55:136–146.

Falangola MF, Jensen JH, Babb JS, Hu C, Castellanos FX, Di Martino A, Ferris SH, Helpern JA. 2008. Age-related non-Gaussian diffusion patterns in the prefrontal brain. J Magn Reson Imaging 28:1345–1350.

Filippi M, Rocca MA. 2004. Magnetization transfer magnetic resonance imaging in the assessment of neurological diseases. J Neuroimaging 14:303–313.

Filippi M, Rocca MA, Falini A, Caputo D, Ghezzi A, Colombo B, Scotti G, Comi G. 2002. Correlations between structural CNS damage and functional MRI changes in primary progressive MS. Neuroimage 15:537–546.

Filippi M, Tortorella C, Rovaris M, Bozzali M, Possa F, Sormani MP, Iannucci G, Comi G. 2000. Changes in the normal appearing brain tissue and cognitive impairment in multiple sclerosis. J Neurol Neurosurg Psychiatry 68:157–161.

Fillard P, Descoteaux M, Goh A, Gouttard S, Jeurissen B, Malcolm J, Ramirez-Manzanares A, Reisert M, Sakaie K, Tensaouti F, Yo T, Mangin JF, Poupon C. 2011. Quantitative evaluation of 10 tractography algorithms on a realistic diffusion MR phantom. Neuroimage 56:220–234.

Fillard P, Poupon C, Mangin JF. 2009. A novel global tractography algorithm based on an adaptive spin glass model. MICCAI Med Image Comput Comput Assist Interv 12:927–934.

Foong J, Symms MR, Barker GJ, Maier M, Woermann FG, Miller DH, Ron MA. 2001. Neuropathological abnormalities in schizophrenia: evidence from magnetization transfer imaging. Brain 124:882–892.

Frank LR. 2002. Characterization of anisotropy in high angular resolution diffusion-weighted MRI. Magn Reson Med 47:1083–1099.

Gao W, Lin W, Chen Y, Gerig G, Smith JK, Jewells V, Gilmore JH. 2009. Temporal and spatial development of axonal maturation and myelination of white matter in the developing brain. AJNR Am J Neuroradiol 30:290–296.

Gochberg DF, Gore JC. 2003. Quantitative imaging of magnetization transfer using an inversion recovery sequence. Magn Reson Med 49:501–505.

Gochberg DF, Kennan RP, Robson MD, Gore JC. 1999. Quantitative imaging of magnetization transfer using multiple selective pulses. Magn Reson Med 41:1065–1072.

Goebell E, Fiehler J, Ding XQ, Paustenbach S, Nietz S, Heese O, Kucinski T, Hagel C, Westphal M, Zeumer H. 2006. Disarrangement of fiber tracts and decline of neuronal density correlate in glioma patients—a combined diffusion tensor imaging and 1H-MR spectroscopy study. AJNR. Am J Neuroradiol 27:1426–1431.

Gong G, Rosa-Neto P, Carbonell F, Chen ZJ, He Y, Evans AC. 2009. Age- and gender-related differences in the cortical anatomical network. J Neurosci Off J Soc Neurosci 29:15684–15693.

Hagmann P, Cammoun L, Gigandet X, Meuli R, Honey CJ, Wedeen VJ, Sporns O. 2008. Mapping the structural core of human cerebral cortex. PLoS Biol 6:e159.

Hagmann P, Kurant M, Gigandet X, Thiran P, Wedeen VJ, Meuli R, Thiran JP. 2007. Mapping human whole-brain structural networks with diffusion MRI. PLoS One 2:e597.

Hagmann P, Sporns O, Madan N, Cammoun L, Pienaar R, Wedeen VJ, Meuli R, Thiran JP, Grant PE. 2010. White matter maturation reshapes structural connectivity in the late developing human brain. Proc Natl Acad Sci U S A 107:19067–19072.

Helms G, Dathe H, Kallenberg K, Dechent P. 2008. High-resolution maps of magnetization transfer with inherent correction for RF inhomogeneity and T1 relaxation obtained from 3D FLASH MRI. Magn Reson Med 60:1396–1407.

Henkelman RM, Stanisz GJ, Graham SJ. 2001. Magnetization transfer in MRI: a review. NMR Biomed 14:57–64.

Hickman SJ, Toosy AT, Jones SJ, Altmann DR, Miszkiel KA, MacManus DG, Barker GJ, Plant GT, Thompson AJ, Miller DH. 2004. Serial magnetization transfer imaging in acute optic neuritis. Brain 127:692–700.

Homer J, Beevers MS. 1985. Driven-equilibrium single-pulse observation of T1 relaxation—a reevaluation of a rapid new method for determining Nmr spin-lattice relaxation-times. J Magn Reson 63:287–297.

Honey CJ, Kotter R, Breakspear M, Sporns O. 2007. Network structure of cerebral cortex shapes functional connectivity on multiple time scales. Proc Natl Acad Sci U S A 104:10240–10245.

Horsfield MA, Barker GJ, Barkhof F, Miller DH, Thompson AJ, Filippi M. 2003. Guidelines for using quantitative magnetization transfer magnetic resonance imaging for monitoring treatment of multiple sclerosis. J Magn Reson Imaging 17:389–397.

Hosseinbor AP, Chung MK, Wu YC, Alexander AL. 2011. Bessel Fourier orientation reconstruction: an analytical EAP reconstruction using multiple shell acquisitions in diffusion MRI. MICCAI Med Image Comput Comput Assist Interv 14(Pt 2):217–225.

Hurley SA, Mossahebi PM, Samsonov AA, Alexander AL, Deoni SC, Fisher R, Duncan ID, Field AS. Multicomponent Relaxometry (mcDESPOT) in the Shaking Pup Model of Dysmyelination. In Proceedings of the 18th Annual Meeting of ISMRM, Stockholm, Sweden, 2010, p. 4516.

Jansen JF, Stambuk HE, Koutcher JA, Shukla-Dave A. 2010. Non-gaussian analysis of diffusion-weighted MR imaging in head and neck squamous cell carcinoma: a feasibility study. AJNR Am J Neuroradiol 31:741–748.

Jellison BJ, Field AS, Medow J, Lazar M, Salamat MS, Alexander AL. 2004. Diffusion tensor imaging of cerebral white matter: a pictorial review of physics, fiber tract anatomy, and tumor imaging patterns. AJNR Am J Neuroradiol 25:356–369.

Jensen JH, Helpern JA, Ramani A, Lu H, Kaczynski K. 2005. Diffusional kurtosis imaging: the quantification of non-gaussian water diffusion by means of magnetic resonance imaging. Magn Reson Med 53:1432–1440.

Jones DK. 2011. *Diffusion MRI. Theory, Methods, and Applications*. New York, NY: Oxford University Press.

Jones DK, Basser PJ. 2004. "Squashing peanuts and smashing pumpkins": how noise distorts diffusion-weighted MR data. Magn Reson Med 52:979–993.

Kabani NJ, Sled JG, Chertkow H. 2002a. Magnetization transfer ratio in mild cognitive impairment and dementia of Alzheimer's type. Neuroimage 15:604–610.

Kabani NJ, Sled JG, Shuper A, Chertkow H. 2002b. Regional magnetization transfer ratio changes in mild cognitive impairment. Magn Reson Med 47:143–148.

Kiefer C, Slotboom J, Buri C, Gralla J, Remonda L, Dierks T, Strik WK, Schroth G, Kalus P. 2004. Differentiating hippocampal subregions by means of quantitative magnetization transfer and relaxometry: preliminary results. Neuroimage 23:1093–1099.

Kier EL, Staib LH, Davis LM, Bronen RA. 2004a. MR imaging of the temporal stem: anatomic dissection tractography of the uncinate fasciculus, inferior occipitofrontal fasciculus, and Meyer's loop of the optic radiation. AJNR Am J Neuroradiol 25:677–691.

Kier EL, Staib LH, Davis LM, Bronen RA. 2004b. Anatomic dissection tractography: a new method for precise MR localization of white matter tracts. AJNR Am J Neuroradiol 25:670–676.

Kim J, Choi IY, Michaelis ML, Lee P. 2011. Quantitative in vivo measurement of early axonal transport deficits in a triple transgenic mouse model of Alzheimer's disease using manganese-enhanced MRI. Neuroimage 56:1286–1292.

Kimura H, Grossman RI, Lenkinski RE, Gonzalez-Scarano F. 1996. Proton MR spectroscopy and magnetization transfer ratio in multiple sclerosis: correlative findings of active versus irreversible plaque disease. AJNR Am J Neuroradiol 17:1539–1547.

Kinoshita M, Yamada K, Hashimoto N, Kato A, Izumoto S, Baba T, Maruno M, Nishimura T, Yoshimine T. 2005. Fiber-tracking does not accurately estimate size of fiber bundle in pathological condition: initial neurosurgical experience using neuronavigation and subcortical white matter stimulation. Neuroimage 25:424–429.

Kitzler HH, Su J, Zeineh M, Harper-Little C, Leung A, Kremenchutzky M, Deoni SC, Rutt BK. 2012. Deficient MWF mapping in multiple sclerosis using 3D whole-brain multi-component relaxation MRI. Neuroimage 59:2670–2677.

Koay CG, Chang LC, Carew JD, Pierpaoli C, Basser PJ. 2006. A unifying theoretical and algorithmic framework for least squares methods of estimation in diffusion tensor imaging. J Magn Reson 182:115–125.

Kreher BW, Mader I, Kiselev VG. 2008. Gibbs tracking: a novel approach for the reconstruction of neuronal pathways. Magn Reson Med 60:953–963.

Kubicki M, Park H, Westin CF, Nestor PG, Mulkern RV, Maier SE, Niznikiewicz M, Connor EE, Levitt JJ, Frumin M, Kikinis R, Jolesz FA, McCarley RW, Shenton ME. 2005. DTI and MTR abnormalities in schizophrenia: analysis of white matter integrity. Neuroimage 26:1109–1118.

Kumar A, Gupta RC, Albert Thomas M, Alger J, Wyckoff N, Hwang S. 2004. Biophysical changes in normal-appearing white matter and subcortical nuclei in late-life major depression detected using magnetization transfer. Psychiatry Res 130:131–140.

Lacomis D, Osbakken M. 1986. Spin-lattice relaxation (T1) times of cerebral white matter in multiple sclerosis—Lacomis −2005- Magnetic Resonance in Medicine—Wiley Online Library. Magn Reson Med 3:194–202.

Lange N, Dubray MB, Lee JE, Froimowitz MP, Froehlich A, Adluru N, Wright B, Ravichandran C, Fletcher PT, Bigler ED, Alexander AL, Lainhart JE. 2010. Atypical diffusion tensor hemispheric asymmetry in autism. Autism Res 3:350–358.

Lawes IN, Barrick TR, Murugam V, Spierings N, Evans DR, Song M, Clark CA. 2008. Atlas-based segmentation of white matter tracts of the human brain using diffusion tensor tractography and comparison with classical dissection. Neuroimage 39:62–79.

Lazar M. 2010. Mapping brain anatomical connectivity using white matter tractography. NMR Biomed 23:821–835.

Lazar M, Alexander AL. 2003. An error analysis of white matter tractography methods: synthetic diffusion tensor field simulations. Neuroimage 20:1140–1153.

Lazar M, Alexander AL. 2005. Bootstrap white matter tractography (BOOT-TRAC). Neuroimage 24:524–532.

Le Bihan D, Moonen CT, van Zijl PC, Pekar J, DesPres D. 1991a. Measuring random microscopic motion of water in tissues with MR imaging: a cat brain study. J Comput Assist Tomogr 15:19–25.

Le Bihan D, Turner R, Moonen CT, Pekar J. 1991b. Imaging of diffusion and microcirculation with gradient sensitization: design, strategy, and significance. J Magn Reson Imaging 1:7–28.

Lee JE, Chung MK, Lazar M, DuBray MB, Kim J, Bigler ED, Lainhart JE, Alexander AL. 2009. A study of diffusion tensor imaging by tissue-specific, smoothing-compensated voxel-based analysis. Neuroimage 44:870–883.

Leemans A, Jones DK. 2009. The B-matrix must be rotated when correcting for subject motion in DTI data. Magn Reson Med 61:1336–1349.

Levesque IR, Giacomini PS, Narayanan S, Ribeiro LT, Sled JG, Arnold DL, Pike GB. 2010. Quantitative magnetization transfer and myelin water imaging of the evolution of acute multiple sclerosis lesions. Magn Reson Med 63:633–640.

Lin CP, Tseng WY, Cheng HC, Chen JH. 2001. Validation of diffusion tensor magnetic resonance axonal fiber imaging with registered manganese-enhanced optic tracts. Neuroimage 14:1035–1047.

Liu C, Li W, Wu B, Jiang Y, Johnson GA. 2012. 3D fiber tractography with susceptibility tensor imaging. Neuroimage 59:1290–1298.

Liu F, Vidarsson L, Winter JD, Tran H, Kassner A. 2010. Sex differences in the human corpus callosum microstructure: a combined T2 myelin-water and diffusion tensor magnetic resonance imaging study. Brain Res 1343:37–45.

Liu IC, Chiu CH, Chen CJ, Kuo LW, Lo YC, Tseng WY. 2010. The microstructural integrity of the corpus callosum and associated impulsivity in alcohol dependence: a tractography-based segmentation study using diffusion spectrum imaging. Psychiatry Res 184:128–134.

Lo CY, Wang PN, Chou KH, Wang J, He Y, Lin CP. 2010. Diffusion tensor tractography reveals abnormal topological organization in structural cortical networks in Alzheimer's disease. J Neurosci Off J Soc Neurosci 30:16876–16885.

Lo YC, Soong WT, Gau SS, Wu YY, Lai MC, Yeh FC, Chiang WY, Kuo LW, Jaw FS, Tseng WY. 2011. The loss of asymmetry and reduced interhemispheric connectivity in adolescents with autism: a study using diffusion spectrum imaging tractography. Psychiatry Res 192:60–66.

Look DC, Locker DR. 1970. Time saving in measurement of NMR and EPR relaxation times. Rev Sci Instrum 41:250–251.

Lori NF, Akbudak E, Shimony JS, Cull TS, Snyder AZ, Guillory RK, Conturo TE. 2002. Diffusion tensor fiber tracking of human brain connectivity: aquisition methods, reliability analysis and biological results. NMR Biomed 15:494–515.

Lori NF, Conturo TE, Le Bihan D. 2003. Definition of displacement probability and diffusion time in q-space magnetic resonance measurements that use finite-duration diffusion-encoding gradients. J Magn Reson 165:185–195.

Lu H, Jensen JH, Ramani A, Helpern JA. 2006. Three-dimensional characterization of non-gaussian water diffusion in humans using diffusion kurtosis imaging. NMR Biomed 19:236–247.

MacKay A, Whittall K, Adler J, Li D, Paty D, Graeb D. 1994. In vivo visualization of myelin water in brain by magnetic resonance. Magn Reson Med 31:673–677.

Mädler B, MacKay AL. In-Vivo 3D Multi-component T2-Relaxation Measurements for Quantitative Myelin Imaging at 3T. In Proceedings of the 14th Annual Meeting of ISMRM, Seattle, WA, 2006, p. 2112.

Mair RW, Sen PN, Hurlimann MD, Patz S, Cory DG, Walsworth RL. 2002. The narrow pulse approximation and long length scale determination in xenon gas diffusion NMR studies of model porous media. J Magn Reson 156:202–212.

Mandl RC, Schnack HG, Luigjes J, van den Heuvel MP, Cahn W, Kahn RS, Hulshoff Pol HE. 2010. Tract-based analysis of magnetization transfer ratio and diffusion tensor imaging of the frontal and frontotemporal connections in schizophrenia. Schizophr Bull 36:778–787.

McLean MA, Barker GJ. 2006. Concentrations and magnetization transfer ratios of metabolites in gray and white matter. Magn Reson Med 56:1365–1370.

Meiboom S, Gill D. 1958. Modified spin-echo method for measuring nuclear relaxation times. Rev Sci Instrum 29:688.

Menon RS, Allen PS. 1991. Application of continuous relaxation time distributions to the fitting of data from model systems and excised tissue. Magn Reson Med 20:214–227.

Mori S, Crain BJ, Chacko VP, van Zijl PC. 1999. Three-dimensional tracking of axonal projections in the brain by magnetic resonance imaging. Ann Neurol 45:265–269.

Moseley ME, Kucharczyk J, Asgari HS, Norman D. 1991. Anisotropy in diffusion-weighted MRI. Magn Reson Med 19:321–326.

Mossahebi P, Samsonov A. Rapid and Accurate Variable Flip Angle T1 Mapping with Correction of MT Effects. International Workshop on Advanced White Matter Imaging, Reykyavik, Iceland, 2011.

Moussavi-Biugui A, Stieltjes B, Fritzsche K, Semmler W, Laun FB. 2011. Novel spherical phantoms for Q-ball imaging under in vivo conditions. Magn Reson Med 65:190–194.

Mulkern RV, Gudbjartsson H, Westin CF, Zengingonul HP, Gartner W, Guttmann CR, Robertson RL, Kyriakos W, Schwartz R, Holtzman D, Jolesz FA, Maier SE. 1999. Multi-component apparent diffusion coefficients in human brain. NMR Biomed 12:51–62.

Murayama Y, Weber B, Saleem KS, Augath M, Logothetis NK. 2006. Tracing neural circuits in vivo with Mn-enhanced MRI. Magn Reson Imaging 24:349–358.

Niendorf T, Dijkhuizen RM, Norris DG, van Lookeren Campagne M, Nicolay K. 1996. Biexponential diffusion attenuation in various states of brain tissue: implications for diffusion-weighted imaging. Magn Reson Med 36:847–857.

Nitkunan A, McIntyre DJ, Barrick TR, O'Sullivan M, Shen Y, Clark CA, Howe FA, Markus HS. 2006. Correlations between MRS and DTI in cerebral small vessel disease. NMR Biomed 19:610–616.

Norris DG, Niendorf T, Hoehn-Berlage M, Kohno K, Schneider EJ, Hainz P, Hropot M, Leibfritz D. 1994. Incidence of apparent restricted diffusion in three different models of cerebral infarction. Magn Reson Imaging 12:1175–1182.

Ou X, Gochberg DF. 2008. MT effects and T1 quantification in single-slice spoiled gradient echo imaging. Magn Reson Med 59:835–845.

Ou X, Sun SW, Liang HF, Song SK, Gochberg DF. 2009. The MT pool size ratio and the DTI radial diffusivity may reflect the myelination in shiverer and control mice. NMR Biomed 22:480–487.

Oweida AJ, Dunn EA, Foster PJ. 2004. Cellular imaging at 1.5 T: detecting cells in neuroinflammation using active labeling with superparamagnetic iron oxide. Mol Imaging 3:85–95.

Pajevic S, Pierpaoli C. 1999. Color schemes to represent the orientation of anisotropic tissues from diffusion tensor data: application to white matter fiber tract mapping in the human brain. Magn Reson Med 42:526–540.

Parker GJ, Haroon HA, Wheeler-Kingshott CA. 2003. A framework for a streamline-based probabilistic index of connectivity (PICo) using a structural interpretation of MRI diffusion measurements. J Magn Reson Imaging 18:242–254.

Perrin M, Poupon C, Rieul B, Leroux P, Constantinesco A, Mangin JF, Lebihan D. 2005. Validation of q-ball imaging with a diffusion fibre-crossing phantom on a clinical scanner. Philos Trans R Soc Lond B Biol Sci 360:881–891.

Pierpaoli C, Barnett A, Pajevic S, Chen R, Penix LR, Virta A, Basser P. 2001. Water diffusion changes in Wallerian degeneration and their dependence on white matter architecture. Neuroimage 13:1174–1185.

Pierpaoli C, Basser PJ. 1996. Toward a quantitative assessment of diffusion anisotropy. Magn Reson Med 36:893–906.

Pike GB, De Stefano N, Narayanan S, Worsley KJ, Pelletier D, Francis GS, Antel JP, Arnold DL. 2000. Multiple sclerosis: magnetization transfer MR imaging of white matter before lesion appearance on T2-weighted images. Radiology 215:824–830.

Poupon C, Rieul B, Kezele I, Perrin M, Poupon F, Mangin JF. 2008. New diffusion phantoms dedicated to the study and validation of high-angular-resolution diffusion imaging (HARDI) models. Magn Reson Med 60:1276–1283.

Pykett IL, Rosen BR, Buonanno FS, Brady TJ. 1983. Measurement of spin-lattice relaxation times in nuclear magnetic resonance imaging. Phys Med Biol 28:723–729.

Raab P, Hattingen E, Franz K, Zanella FE, Lanfermann H. 2010. Cerebral gliomas: diffusional kurtosis imaging analysis of microstructural differences. Radiology 254:876–881.

Rademacher J, Engelbrecht V, Burgel U, Freund H, Zilles K. 1999. Measuring in vivo myelination of human white matter fiber

tracts with magnetization transfer MR. Neuroimage 9:393–406.
Roberts TP, Liu F, Kassner A, Mori S, Guha A. 2005. Fiber density index correlates with reduced fractional anisotropy in white matter of patients with glioblastoma. AJNR Am J Neuroradiol 26:2183–2186.
Rocca MA, Agosta F, Martinelli V, Falini A, Comi G, Filippi M. 2006. The level of spinal cord involvement influences the pattern of movement-associated cortical recruitment in patients with isolated myelitis. Neuroimage 30:879–884.
Ropele S, Filippi M, Valsasina P, Korteweg T, Barkhof F, Tofts PS, Samson R, Miller DH, Fazekas F. 2005. Assessment and correction of B1-induced errors in magnetization transfer ratio measurements. Magn Reson Med 53:134–140.
Ropele S, Seifert T, Enzinger C, Fazekas F. 2003. Method for quantitative imaging of the macromolecular 1H fraction in tissues. Magn Reson Med 49:864–871.
Rovaris M, Agosta F, Sormani MP, Inglese M, Martinelli V, Comi G, Filippi M. 2003. Conventional and magnetization transfer MRI predictors of clinical multiple sclerosis evolution: a medium-term follow-up study. Brain 126:2323–2332.
Rovaris M, Filippi M, Falautano M, Minicucci L, Rocca MA, Martinelli V, Comi G. 1998. Relation between MR abnormalities and patterns of cognitive impairment in multiple sclerosis. Neurology 50:1601–1608.
Rubinov M, Sporns O. 2010. Complex network measures of brain connectivity: uses and interpretations. Neuroimage 52:1059–1069.
Sacolick LI, Wiesinger F, Hancu I, Vogel MW. 2010. B1 mapping by Bloch-Siegert shift. Magn Reson Med 63:1315–1322.
Saleem KS, Pauls JM, Augath M, Trinath T, Prause BA, Hashikawa T, Logothetis NK. 2002. Magnetic resonance imaging of neuronal connections in the macaque monkey. Neuron 34:685–700.
Samson RS, Wheeler-Kingshott CA, Symms MR, Tozer DJ, Tofts PS. 2006. A simple correction for B1 field errors in magnetization transfer ratio measurements. Magn Reson Imaging 24:255–263.
Santos AC, Narayanan S, de Stefano N, Tartaglia MC, Francis SJ, Arnaoutelis R, Caramanos Z, Antel JP, Pike GB, Arnold DL. 2002. Magnetization transfer can predict clinical evolution in patients with multiple sclerosis. J Neurol 249:662–668.
Sati P, Silva AC, van Gelderen P, Gaitan MI, Wohler JE, Jacobson S, Duyn JH, Reich DS. 2012. In vivo quantification of T(2) anisotropy in white matter fibers in marmoset monkeys. Neuroimage 59:979–985.
Schmahmann JD, Pandya DN, Wang R, Dai G, D'Arceuil HE, de Crespigny AJ, Wedeen VJ. 2007. Association fibre pathways of the brain: parallel observations from diffusion spectrum imaging and autoradiography. Brain J Neurol 130: 630–653.
Schmierer K, Scaravilli F, Altmann DR, Barker GJ, Miller DH. 2004. Magnetization transfer ratio and myelin in postmortem multiple sclerosis brain. Ann Neurol 56:407–415.
Schmierer K, Tozer DJ, Scaravilli F, Altmann DR, Barker GJ, Tofts PS, Miller DH. 2007. Quantitative magnetization transfer imaging in postmortem multiple sclerosis brain. J Magn Reson Imaging 26:41–51.
Sibson NR, Lowe JP, Blamire AM, Martin MJ, Obrenovitch TP, Anthony DC. 2008. Acute astrocyte activation in brain detected by MRI: new insights into T(1) hypointensity. J. Cereb Blood Flow Metab 28:621–632.
Silver NC, Barker GJ, Miller DH. 1999. Standardization of magnetization transfer imaging for multicenter studies. Neurology 53:S33–S39.
Sled JG, Pike GB. 2001. Quantitative imaging of magnetization transfer exchange and relaxation properties in vivo using MRI. Magn Reson Med 46:923–931.
Smith RS, Koles ZJ. 1970. Myelinated nerve fibers: computed effect of myelin thickness on conduction velocity. Am J Physiol 219:1256–1258.
Smith SM, Jenkinson M, Johansen-Berg H, Rueckert D, Nichols TE, Mackay CE, Watkins KE, Ciccarelli O, Cader MZ, Matthews PM, Behrens TE. 2006. Tract-based spatial statistics: voxelwise analysis of multi-subject diffusion data. Neuroimage 31:1487–1505.
Song SK, Sun SW, Ramsbottom MJ, Chang C, Russell J, Cross AH. 2002. Dysmyelination revealed through MRI as increased radial (but unchanged axial) diffusion of water. Neuroimage 17:1429–1436.
Sporns O, Tononi G, Kotter R. 2005. The human connectome: a structural description of the human brain. PLoS Comput Biol 1:e42.
Stanisz GJ, Kecojevic A, Bronskill MJ, Henkelman RM. 1999. Characterizing white matter with magnetization transfer and T(2). Magn Reson Med 42:1128–1136.
Stanisz GJ, Webb S, Munro CA, Pun T, Midha R. 2004. MR properties of excised neural tissue following experimentally induced inflammation. Magn Reson Med 51:473–479.
Stejskal E, Tanner JE. 1965. Diffusion measurements: spin echoes in the presence of a time-dependent field gradient. J Chem Phys 42:288–292.
Stewart WA, MacKay AL, Whittall KP, Moore GR, Paty DW. 1993. Spin-spin relaxation in experimental allergic encephalomyelitis. Analysis of CPMG data using a non-linear least squares method and linear inverse theory. Magn Reson Med 29:767–775.
Stikov N, Perry LM, Mezer A, Rykhlevskaia E, Wandell BA, Pauly JM, Dougherty RF. 2011. Bound pool fractions complement diffusion measures to describe white matter micro and macrostructure. Neuroimage 54:1112–1121.
Sun SW, Liang HF, Le TQ, Armstrong RC, Cross AH, Song SK. 2006. Differential sensitivity of in vivo and ex vivo diffusion tensor imaging to evolving optic nerve injury in mice with retinal ischemia. Neuroimage 32:1195–1204.
Tofts P. 2003. *Quantitative MRI of the brain: Measuring Changes Caused by Disease*. Chichester, West Sussex: Wiley.
Tofts PS, Steens SC, Cercignani M, Admiraal-Behloul F, Hofman PA, van Osch MJ, Teeuwisse WM, Tozer DJ, van Waesberghe JH, Yeung R, Barker GJ, van Buchem MA. 2006. Sources of variation in multi-centre brain MTR histogram studies: body-coil transmission eliminates inter-centre differences. MAGMA 19:209–222.
Tournier JD, Calamante F, Gadian DG, Connelly A. 2004. Direct estimation of the fiber orientation density function from diffusion-weighted MRI data using spherical deconvolution. Neuroimage 23:1176–1185.
Tournier JD, Mori S, Leemans A. 2011. Diffusion tensor imaging and beyond. Magn Reson Med 65:1532–1556.
Tozer D, Ramani A, Barker GJ, Davies GR, Miller DH, Tofts PS. 2003. Quantitative magnetization transfer mapping of bound protons in multiple sclerosis. Magn Reson Med 50:83–91.
Tozer DJ, Davies GR, Altmann DR, Miller DH, Tofts PS. 2005. Correlation of apparent myelin measures obtained in multiple sclerosis patients and controls from magnetization transfer and multicompartmental T2 analysis. Magn Reson Med 53:1415–1422.
Trampel R, Jensen JH, Lee RF, Kamenetskiy I, McGuinness G, Johnson G. 2006. Diffusional kurtosis imaging in the lung using hyperpolarized 3He. Magn Reson Med 56:733–737.

Trapp BD, Peterson J, Ransohoff RM, Rudick R, Mork S, Bo L. 1998. Axonal transection in the lesions of multiple sclerosis. N Engl J Med 338:278–285.

Tuch DS. 2004. Q-ball imaging. Magn Reson Med 52:1358–1372.

Underhill HR, Rostomily RC, Mikheev AM, Yuan C, Yarnykh VL. 2011. Fast bound pool fraction imaging of the in vivo rat brain: association with myelin content and validation in the C6 glioma model. Neuroimage 54:2052–2065.

Underhill HR, Yuan C, Yarnykh VL. 2009. Direct quantitative comparison between cross-relaxation imaging and diffusion tensor imaging of the human brain at 3.0 T. Neuroimage 47:1568–1578.

van Buchem MA, Grossman RI, Armstrong C, Polansky M, Miki Y, Heyning FH, Boncoeur-Martel MP, Wei L, Udupa JK, Grossman M, Kolson DL, McGowan JC. 1998. Correlation of volumetric magnetization transfer imaging with clinical data in MS. Neurology 50:1609–1617.

van Buchem MA, Steens SC, Vrooman HA, Zwinderman AH, McGowan JC, Rassek M, Engelbrecht V. 2001. Global estimation of myelination in the developing brain on the basis of magnetization transfer imaging: a preliminary study. AJNR Am J Neuroradiol 22:762–766.

Vavasour IM, Whittall KP, MacKay AL, Li DK, Vorobeychik G, Paty DW. 1998. A comparison between magnetization transfer ratios and myelin water percentages in normals and multiple sclerosis patients. Magn Reson Med 40:763–768.

Velikina J, Hurley S, Alexander A, Samsonov AA. Accelerating Multi-Component Relaxometry in Steady State with an Application of Constrained Reconstruction in Parametric Dimension. In Proceedings of the 19th Annual Meeting of ISMRM, Montreal, Quebec, Canada, 2011, p. 2740.

Watanabe M, Aoki S, Masutani Y, Abe O, Hayashi N, Masumoto T, Mori H, Kabasawa H, Ohtomo K. 2006. Flexible ex vivo phantoms for validation of diffusion tensor tractography on a clinical scanner. Radiat Med 24:605–609.

Wedeen VJ, Hagmann P, Tseng WY, Reese TG, Weisskoff RM. 2005. Mapping complex tissue architecture with diffusion spectrum magnetic resonance imaging. Magn Reson Med 54:1377–1386.

Westin CF, Maier SE, Mamata H, Nabavi A, Jolesz FA, Kikinis R. 2002. Processing and visualization for diffusion tensor MRI. Med Image Anal 6:93–108.

Wheeler-Kingshott CA, Cercignani M. 2009. About "axial" and "radial" diffusivities. Magn Reson Med 61:1255–1260.

Whittall K, Mackay A. 1989. Quantitative interpretation of NMR relaxation data. J Magn Reson 84:134–152.

Whittall KP, MacKay AL, Graeb DA, Nugent RA, Li DK, Paty DW. 1997. In vivo measurement of T2 distributions and water contents in normal human brain. Magn Reson Med 37:34–43.

Witwer BP, Moftakhar R, Hasan KM, Deshmukh P, Haughton V, Field A, Arfanakis K, Noyes J, Moritz CH, Meyerand ME, Rowley HA, Alexander AL, Badie B. 2002. Diffusion-tensor imaging of white matter tracts in patients with cerebral neoplasm. J Neurosurg 97:568–575.

Wolff SD, Balaban RS. 1989. Magnetization transfer contrast (MTC) and tissue water proton relaxation in vivo. Magn Reson Med 10:135–144.

Wu YC, Alexander AL. 2007. Hybrid diffusion imaging. Neuroimage 36:617–629.

Wu YC, Field AS, Alexander AL. 2008. Computation of diffusion function measures in q-space using magnetic resonance hybrid diffusion imaging. IEEE Trans Med Imaging 27:858–865.

Wu YC, Field AS, Duncan ID, Samsonov AA, Kondo Y, Tudorascu D, Alexander AL. 2011a. High b-value and diffusion tensor imaging in a canine model of dysmyelination and brain maturation. Neuroimage 58:829–837.

Wu YC, Field AS, Whalen PJ, Alexander AL. 2011b. Age- and gender-related changes in the normal human brain using hybrid diffusion imaging (HYDI). Neuroimage 54:1840–1853.

Yamada M, Momoshima S, Masutani Y, Fujiyoshi K, Abe O, Nakamura M, Aoki S, Tamaoki N, Okano H. 2008. Diffusion-tensor neuronal fiber tractography and manganese-enhanced MR imaging of primate visual pathway in the common marmoset: preliminary results. Radiology 249:855–864.

Yarnykh V. Analytical Method for Correction of B1 Errors in High-Field Magnetization Transfer Ratio Mapping. In Proceedings of the 17th Annual Meeting of ISMRM, Honolulu, HI, 2009, p. 4482.

Yarnykh VL. 2002. Pulsed Z-spectroscopic imaging of cross-relaxation parameters in tissues for human MRI: theory and clinical applications. Magn Reson Med 47:929–939.

Yarnykh VL. 2007. Actual flip-angle imaging in the pulsed steady state: a method for rapid three-dimensional mapping of the transmitted radiofrequency field. Magn Reson Med 57:192–200.

Yarnykh VL. 2010. Optimal radiofrequency and gradient spoiling for improved accuracy of T1 and B1 measurements using fast steady-state techniques. Magn Reson Med 63: 1610–1626.

Yarnykh VL, Yuan C. 2004. Cross-relaxation imaging reveals detailed anatomy of white matter fiber tracts in the human brain. Neuroimage 23:409–424.

Zhang H, Yushkevich PA, Alexander DC, Gee JC. 2006. Deformable registration of diffusion tensor MR images with explicit orientation optimization. Med Image Anal 10:764–785.

Zhang Y, Zhang J, Oishi K, Faria AV, Jiang H, Li X, Akhter K, Rosa-Neto P, Pike GB, Evans A, Toga AW, Woods R, Mazziotta JC, Miller MI, van Zijl PC, Mori S. 2010. Atlas-guided tract reconstruction for automated and comprehensive examination of the white matter anatomy. Neuroimage 52:1289–1301.

Zhuo J, Xu S, Proctor JL, Mullins RJ, Simon JZ, Fiskum G, Gullapalli RP. 2012. Diffusion kurtosis as an in vivo imaging marker for reactive astrogliosis in traumatic brain injury. Neuroimage 59:467–477.

Address correspondence to:
Andrew L. Alexander
Waisman Laboratory for Brain Imaging and Behavior
Waisman Center
1500 Highland Avenue
Madison, WI 53705

E-mail: alalexander2@wisc.edu